On vector field reconstructions for semi-Lagrangian transport methods on geodesic staggered grids

Pedro S. Peixoto, Saulo R.M. Barros *

Instituto de Matemática e Estatística, Universidade de São Paulo, R. do Matão 1010, 05508-090 São Paulo, Brazil

ARTICLE INFO

ABSTRACT

We analyse several vector reconstruction methods, based on the knowledge of only specific pointwise vector components, and extend their use to non-structured polygonal C-grids on the sphere. The emphasis is on the reconstruction of the vector field at arbitrary locations on the sphere, as required by semi-Lagrangian transport schemes. This is done by first reconstructing the vector field to fixed locations, followed by interpolations with generalized barycentric coordinates. We derive a hybrid scheme, combining the efficiency of Perot's method with the accuracy of a least square scheme. This method is second order accurate, and has shown to be competitive and computationally efficient. We analysed the vector reconstruction methods within a semi-Lagrangian transport method, and demonstrated that second order accurate reconstructions are enough to fulfil the requirements for second order accurate semi-Lagrangian methods on icosahedral C-grids.

© 2014 Elsevier Inc. All rights reserved.

1. Introduction

Quasi-uniform geodesic grids have achieved considerable importance in global atmospheric modelling and have been adopted in some recent developed models (e.g. [1,2]). One of the motivations for this choice is that models based on quasi-uniform grids are prone to scale better on massively parallel computers than several operational models making use of latitude–longitude grids [3]. Nevertheless, interesting questions arise in the development of models on quasi-uniform grids, mainly related to their non-orthogonality and lack of structure. In the present work, we shall concentrate on hexagonal/pentagonal icosahedral geodesic C-grids, or generally, on Voronoi like C-grids (including spherical centroidal tessellations [4]). The use of staggering of variables, especially of the C-grid type, favours a better representation of fast waves [3]. The aspects to be emphasised in this work are related to the development of semi-Lagrangian models on icosahedral grids. Semi-Lagrangian schemes, either used as a transport method for moisture and other tracers, or combined with semi-implicit discretizations in dynamical cores, play an important role on many operational atmospheric models. A crucial part in a semi-Lagrangian scheme is an accurate trajectory computation. In the computation of the trajectories, semi-Lagrangian schemes usually require sufficiently good approximations to the wind field at any point on the sphere, based on the available wind information. Usually, only the normal components of the winds at the midpoints of the edges of the Voronoi tessellation will be known (in some schemes, the tangential components may be available instead). The problem of obtaining the wind

---

* Corresponding author. Tel.: +55 11 30916136; fax: +55 11 30916131.
 E-mail addresses: pedrosp@ime.usp.br (P.S. Peixoto), saulo@ime.usp.br (S.R.M. Barros).

field at an arbitrary location from the available wind components is often called the vector field reconstruction problem, focus of this work.

Vector field reconstructions have been considered by Wang et al [5] for triangular C-grids on the plane, in the context of modelling oceanic flows. They have examined the use of finite element based methods (as the Raviart–Thomas (RT) triangular elements [6]), of Perot's methods [7] and of polygonal least square (LSQ) reconstructions [8]. Bonaventura et al. [9] considered the use of radial basis functions (RBF) and compared them to RT reconstructions, showing that RBF based methods outperform the RT schemes on triangular grids. All these schemes have been originally developed for planar triangular grids, with the exception of RBF methods.

The purpose of this paper is to investigate vector reconstruction methods for general spherical polygonal C-grids. We aim to reconstruct the vector fields at arbitrary locations on the sphere, as required in usual semi-Lagrangian trajectory computations [10]. With this objective, we devise ways to extend edge-based finite element methods (such as RT and Whitney [11] elements), Perot's schemes and least square reconstructions to spherical polygonal C-grids and compare their accuracy and computational efficiency, also with the RBF methods.

As observed in [5] for triangular grids, nonuniformity of grid cells influence the accuracy of the methods. The grid properties may affect the precision of the schemes, to the point that interpolation and discretization errors exhibit a marked grid-pattern, what is known as grid-imprinting [12]. We observe this behaviour with the edge-based finite element methods and with Perot's method. In [13] we were able to directly relate the grid-imprinting of finite volume discretizations of the divergence operator to an alignment property (introduced in [13]) of the grid cells. With a similar analysis, we can explain the error patterns of Perot's method. Moreover, with the aid of the cell alignment indexes, we can devise a hybrid reconstruction method, combining the (computationally cheap) method of Perot on well aligned cells with a more expensive least square method, used only on the minority of badly aligned cells. The resulting scheme has similar accuracy to least square methods, at a much lower cost. This hybrid scheme also shows to be competitive to RBF methods using 6 or 9 point stencils, with the advantage of not requiring the precomputation and storage of matrices decompositions. As observed in [9], and well investigated in the literature [14], RBF methods present a certain duality between precision and numerical stability. For fixed size stencils, the condition numbers of the systems to be solved grow very fast for finer grids. For the resolutions in current use, the systems are still stable and RBF methods provide good approximations [1,2], but this may be a potential problem in the way to cloud resolving models. The addition of a polynomial part to the RBF basis may contribute to alleviate this problem. We investigated the use of Gaussian kernels with an extra constant term in the reconstruction of vector fields, with some interesting results concerning the use of variable shape parameters in the radial basis functions.

It is possible to apply the analysed reconstruction schemes directly to any location, possibly with less accuracy, since several methods are more accurate when the reconstruction points are located at the barycenters of the polygonal cells, getting worse near the edges, specially if only nearest neighbours are used in the reconstructions. With wider stencils, LSQ and RBF schemes do not loose accuracy in the reconstructions to arbitrary locations, although the reconstructed field will present discontinuities over the cell edges. An alternative, which ensures global continuity, is the use of the reconstruction algorithms to fixed points (e.g. barycenters or cell nodes), followed by a continuous interpolation from these values. With this latter approach, the order of the reconstruction scheme will be preserved if the interpolation method is chosen accordingly. We derived an extension to the sphere of the generalized Wachspress barycentric coordinates [15,16], sufficient to maintain second order accuracy and to ensure global continuity, which is adequate for the schemes considered in the paper.

Vector reconstructions may be used in different contexts, such as for data assimilation methods or visualization algorithms. Our principal interest is their use on semi-Lagrangian schemes, specially on tracer transport methods. Our focus is on traditional interpolating semi-Lagrangian schemes [10], although our analysis may be applicable to cell oriented conservative semi-Lagrangian transport schemes (as in [17] or [18]) which rely on accurate trajectory computations. We show that the requirements for a globally second order scheme involve the computation of trajectories with third order accuracy. A vector reconstruction method of at least second order will be necessary for that, if the trajectories are computed with traditional schemes such as Robert's method [19]. We tested a two-time-level semi-Lagrangian advection scheme on geodesic icosahedral C-grids. We analysed the precision of the trajectories approximations and the overall accuracy of the scheme, employing a deformational test flow suggested in [20]. The adequacy of the hybrid scheme for vector reconstructions has been demonstrated.

The paper is organized as follows. In Section 2 we analyse and extend existing vector reconstruction methods to spherical polygonal C-grids. Section 3 is devoted to the proposed hybrid reconstruction scheme, which is compared to the other methods, including tests on a locally refined Voronoi tessellation. Section 4 is dedicated to tests with the semi-Lagrangian advection method. We close the paper in Section 5 with some final remarks. The analysis of Perot's method on aligned cells is presented in Appendix A. Appendix B contains details about the addition of a polynomial part in RBF vector reconstruction methods. The accuracy requirements for our semi-Lagrangian scheme are derived in Appendix C.

2. Vector reconstruction methods

Let $\{u_i\}_{i=1,\dots,n}$ be the components of a vector field, $\vec{u}$, normal to given grid edges at their midpoints. The vector reconstruction problem is how to obtain a vector field $\vec{u}_h$ that approximates $\vec{u}$, based on the known values u_i. Usually $\vec{u}_h$ is required to satisfy the interpolatory conditions

$$\vec{u}_h(\vec{x}_i) \cdot \vec{n}_i = u_i, \quad i = 1, ..., n, \tag{1}$$

where $\vec{n}_i$ is an unitary normal vector to the i-th edge of a set of edges whose midpoints are denoted $\vec{x}_i$.

One may consider this vector reconstruction problem either based on local or on global information. For atmospheric models the local methods are generally adequate, and therefore will be the focus of our work. More specifically, we concentrate on local vector reconstructions for Voronoi-like C grids. In this case, the computational cells have an arbitrary polygonal shape (usually a pentagon or hexagon) and the vector normal components are assumed to be known at the midpoints of the edges.

Before the presentation of the several reconstruction methods, we describe how barycentric coordinates may be generalized to polygons on the sphere. These spherical barycentric coordinates provide an efficient second order interpolation scheme, which, once the reconstruction to cell vertices or cell centers is performed, will be used to obtain the vector field at any location on the sphere.

2.1. Spherical barycentric coordinates

General barycentric coordinates are a powerful tool for interpolation on arbitrary polygons. For a planar triangle, the barycentric coordinates are uniquely defined, whereas for general polygons this is not the case. Several general barycentric coordinates systems have been proposed in the literature. Among them we point out the Wachspress coordinates [15] and the mean value coordinates [21], well suited for local interpolation methods. A detailed comparison of barycentric coordinates was made in [16]. For our purposes, aiming at their use on Voronoi grids, we only consider coordinates for convex polygons.

For a planar convex polygon Ω with n vertices, a general barycentric coordinate system is a set of functions, $\{\lambda_i\}$, $i = 1, ..., n$, $\lambda : \Omega \to \mathbb{R}$, satisfying the properties of linear exactness,

$$\vec{x} = \sum_{i=1}^{n} \lambda_i(\vec{x}) \vec{c}_i, \tag{2}$$

partition of unity,

$$\sum_{i=1}^{n} \lambda_i(\vec{x}) = 1, \tag{3}$$

and interpolation,

$$\lambda_i(\vec{c}_j) = \delta_{ij}, \tag{4}$$

where $\vec{c}_i$ is a vertex of the polygon (see Fig. 1) and δ_{ij} is the Kronecker's delta function ($\delta_{ij} = 1$ if $i = j$ and zero otherwise).

If f is a linear, scalar or vector function, known at the vertices of the polygon, it may then be written as

$$f(\vec{x}) = \sum_{i=1}^{n} \lambda_i(\vec{x}) f(\vec{c}_i). \tag{5}$$

As a result, if the coordinates $\lambda_i(\vec{x})$ are used as weights for interpolating values given at the polygon vertices, the method is exact for linear functions. It follows that for general smooth functions it is a second order method.

The Wachspress coordinates are defined as

$$\lambda_i(\vec{x}) = \frac{w_i(\vec{x})}{\sum_{j=1}^{n} w_j(\vec{x})}, \tag{6}$$

where

$$w_i(\vec{x}) = B_i \prod_{j \neq i-1, i} A_j(\vec{x}), \tag{7}$$

B_i is the area of the triangle formed by the vertices $\{\vec{c}_{i-1}, \vec{c}_i, \vec{c}_{i+1}\}$, and $A_j(\vec{x})$ is the area of the triangle formed by the vertices $\{\vec{c}_{i-1}, \vec{c}_i\}$ and the point $\vec{x}$ (see Fig. 1). For numerical stability, it is convenient to use normalized areas, that is, the areas of the triangles divided by the polygon area ($A_i/|\Omega|$ and $B_i/|\Omega|$). When we have a triangle, these coordinates reduce to the usual barycentric coordinates.

Extensions of generalized barycentric coordinates to the sphere have been investigated in [22] and [23]. They realized that such type of coordinates cannot simultaneously satisfy the partition of unity and the linearity properties on the sphere. The choice made in both [22] and [23] was to relax the partition of unity, and ensure linearity. The undesirable consequence of this approach is that the interpolation method will not reproduce exactly constant functions. Therefore, we rather relax the linearity property, and preserve the partition of unity. In order to achieve this, we employ the areas of the spherical
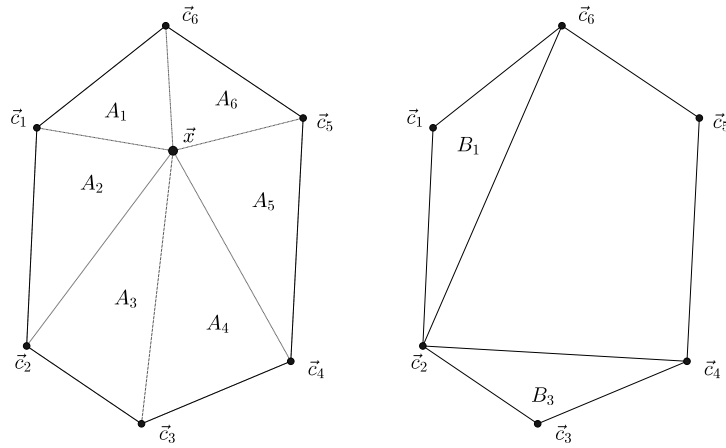
Fig. 1. Notation used in Wachspress coordinates.

triangles in definition (6), obtaining a spherical Wachspress method. Linearity is obtained at the edges, as well as continuity across edges of contiguous cells.

The spherical general barycentric coordinates are well defined in this way for scalar interpolations with data given on the polygon vertices. However, linear combinations of vectors tangent to the sphere at given places of the polygon will normally not belong to the tangent plane at the interpolation point. Therefore, the resulting vector is projected onto this plane. Our numerical results indicate that this procedure preserves second order accuracy on arbitrary spherical polygons.

2.2. Reconstruction to arbitrary points

In order to obtain a vector field at an arbitrary point on the sphere we proceed in two steps. From the known vector components at grid edges, we first compute the vector field at specific grid points. These values are then interpolated to obtain the vector field at any location. In the first step we consider the possibilities:

- Vector Reconstruction to Triangle Vertices (VRTV),
- Vector Reconstruction to Voronoi cell Barycenters (VRVB).
- Vector Reconstruction to Triangle Circumcenters (VRTC).
- Vector Reconstruction to Triangle Barycenters (VRTB).

In the second step the spherical Wachspress coordinates are used for the vector interpolation. Notice that, on the sphere, barycenters have to be defined as the constrained centroids, as in [24]. Reconstruction to cell centroids may be more accurate with some methods, but the orthogonality relation between triangle edges and Voronoi cell edges may be lost, what is relevant for some models (e.g. [25]), but less for others (e.g. [26]).

2.3. Edge-based basis reconstructions

#### a) Planar triangular edge-based elements

Raviart and Thomas [6] proposed finite elements vector basis, which were based on information of the vector fields at the edges of the cell elements. The zero-th order Raviart–Thomas (RT0) triangular element defines a linear vector field basis that has unitary normal component on a reference edge and is tangent to the other edges [27]. Such basis is interesting for vector reconstructions on triangles when the normal components are known at the edge midpoints, as shown in [5]. This approach ensures a reconstructed vector field that exactly reproduces constant, and linear non-divergent, vector fields.

Whitney [11] proposed a finite element basis similar to the RT0 element, but having a unitary tangent vector at the midpoint of one of the triangle edges, while being normal to the other two edges. This basis may be written using barycentric coordinates in the following way [28],

$$\vec{\psi}_i(\vec{x}) = \frac{\lambda_{i-1}(\vec{x})\,\vec{n}_{i+1}}{\vec{n}_{i+1} \cdot \vec{t}_i} + \frac{\lambda_{i+1}(\vec{x})\,\vec{n}_{i-1}}{\vec{n}_{i-1} \cdot \vec{t}_i}, \tag{8}$$

where $\vec{t}_i$ is the unitary tangent vector (defined in counter-clockwise direction) and $\vec{n}_i$ is the outer unitary normal vector with respect to the i-th triangle edge, $\lambda_i(\vec{x})$ is the barycentric coordinate of $\vec{x}$ relative to the vertex i, opposed to edge i, and we identify the vertices in a cyclic way. We have that

$$\vec{\psi}_i(\vec{x}_j) \cdot \vec{t}_j = \delta_{ij}, \tag{9}$$
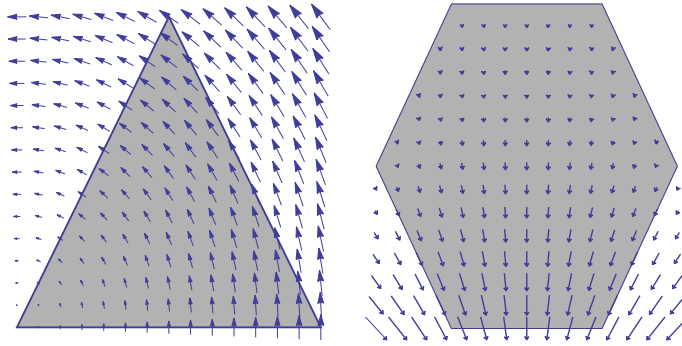
Fig. 2. Example of Whitney vector basis for the top right edge of a triangle (left). Example of edge based basis for the bottom edge of a hexagon (right).
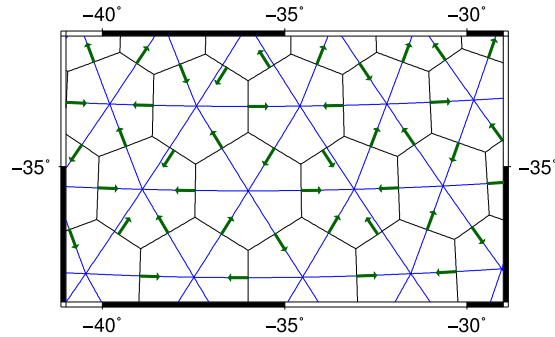
Fig. 3. Region of an icosahedral grid level 5 illustrating triangular and Voronoi cells. The arrows are vectors normal to Voronoi cell edge midpoints. The directions of the vectors were chosen arbitrarily.

where $\vec{x}_j$ is any point on the j-th edge (note that $\lambda_i(\vec{x}_j) = 0$ if $i \neq j$). We illustrate one element of this basis in Fig. 2. This basis reproduces exactly constant vector fields and also linear vector fields with null curl. In general, only a first order approximation is ensured.

On a Voronoi C grid, the Voronoi cell normal components are approximately the tangent components of the triangular cells (see Fig. 3). The midpoints of the Voronoi cell edges do not coincide with the triangle edge midpoints, but they are a first order approximation. Thus, the Whitney basis can be used on the triangular cells to reconstruct to the circumcenters (VRTC), or to the triangle barycenters (VRTB), resulting in a first order approximation method. Given the normal edge components (u_i) of the Voronoi cells, relative to the 3 triangle edges, the reconstructed vector field may be written as

$$\vec{u}(\vec{x}) = \sum_{i=1}^{3} u_i \vec{\psi}_i(\vec{x}), \tag{10}$$

which will be denoted as Whitney method using 3 edges (WT3), referring to triangle edges.

b) Planar polygonal edge-based elements

Recently, Klausen et al. [29] described a way to extend the RT0 element to convex shaped polygons using generalized barycentric coordinates. The method results in an edge-based vector basis (EBB). For a given edge i of a planar polygon Ω, the vector basis function is defined as

$$\vec{\phi}_i(\vec{x}) = \frac{\vec{t}_{i-1}}{2B_i} \lambda_i(\vec{x}) - \frac{\vec{t}_{i+1}}{2B_{i+1}} \lambda_{i+1}(\vec{x}) \tag{11}$$

where $\vec{t}_j$ is the unit vector tangent to the jth edge pointing in the counter-clockwise direction, λ_j is a general barycentric coordinate relative to vertex j, and B_j is the area of the triangle formed by the vertices $\{\vec{c}_{j-1}, \vec{c}_j, \vec{c}_{j+1}\}$ (cf. Fig. 4(a)).

If the polygon is a triangle, the RT0 element is obtained. Each basis function satisfies the property

$$\vec{\phi}_i(\vec{x}_j) \cdot \vec{n}_j = \delta_{ij}. \tag{12}$$

In Fig. 2 we illustrate the basis function for one edge of a hexagon.

Given the normal edge components (u_i) of a vector field relative to a polygon with n edges, the reconstructed vector field will be written as
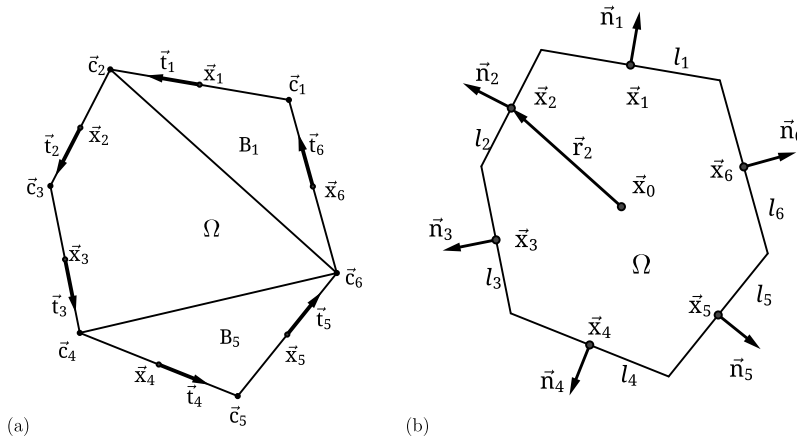
Fig. 4. Indexation used for (a) edge-based basis and (b) Perot's reconstruction methods.

$$\vec{u}(\vec{x}) = \sum_{i=1}^{n} u_i \vec{\phi}_i(\vec{x}), \tag{13}$$

where, $\vec{x}$ is an arbitrary interpolation point inside the polygon. We denote this method as Edge-Based with 6 edges (EB6), as usually the reconstruction will be applied to hexagonal shaped polygons. It is exact for constant (planar) vector fields.

c) Edge-based methods on the sphere

It is possible to define spherical edge-based elements, analogous to the planar elements, using vectors pointwise tangent to the sphere. For instance, an extension of the RT0 element can be defined on a spherical triangle, such that at a given reference edge, the vector field has unitary normal components. At the opposite vertex to this edge it would have null value. Along the geodesics joining the opposite vertex to the given edge, the tangent vectors follow the geodesic and have a linearly varying magnitude (from zero at the opposite vertex till its value at the reference edge, at the position the geodesic intercepts it). In this way, the resulting vector field is also tangent to the other edges of the triangle.

However, we did not find a practical way to express these spherical elements, in order to use them in reconstruction methods. Instead, in order to apply the edge-based elements on the sphere, we use an ad hoc extension. In the definitions (8) and (11) we employ the spherical Wachspress barycentric coordinates. We observe that we combine vectors which are tangent to the sphere on different locations and therefore do not belong to the same plane. These linear combinations are evaluated in $\mathbb{R}^3$ and the resulting vector is orthogonally projected onto the plane of tangency to the sphere at the reconstruction location.

2.4. Perot's method

Perot [7] used the divergence theorem to deduce formulas to reconstruct a vector field at an interior point of a polygon using either normal or tangential components of the vector field, given at the edge midpoints of the polygon.

a) Reconstruction using normal vectors

We first review the construction of the method on a plane. Given a vector field $\vec{u}$, let $\vec{v} = (\vec{a} \cdot \vec{r})\vec{u}$, where $\vec{a}$ is a constant vector, $\vec{r} = \vec{x} - \vec{x}_0$, with $\vec{x}_0$ being an interior point of a polygon Ω, and $\vec{u}$ a vector field. Then

$$\int_{\Omega} \operatorname{div}(\vec{v}) \, dA \;=\; \int_{\partial \Omega} \vec{v} \cdot \vec{n} \, dl$$

$$\Longleftrightarrow$$

$$\int_{\Omega} \operatorname{div}\big((\vec{a} \cdot \vec{r})\vec{u}\big) \, dA \;=\; \sum_{i=1}^{n} \int_{\gamma_i} (\vec{a} \cdot \vec{r})(\vec{u} \cdot \vec{n}_i) \, dl$$

$$\Longleftrightarrow$$

$$\vec{a} \cdot \left(\int_{\Omega} \big(\vec{u} + \vec{r} \operatorname{div}(\vec{u})\big) \, dA \right) \;=\; \vec{a} \cdot \left(\sum_{i=1}^{n} \int_{\gamma_i} \vec{r}(\vec{u} \cdot \vec{n}_i) \, dl \right) \tag{14}$$

where γ_i is the ith edge of Ω and $\vec{n}_i$ is the edge unitary outer normal vector. If we assume that $\vec{u} = \vec{u}_0$, with $\vec{u}_0$ being a constant vector, then $\operatorname{div}(\vec{u}) = 0$ and

$$\vec{u}_0 = \frac{1}{|\Omega|} \sum_{i=1}^{n} \vec{r}_i \, u_i \, l_i, \tag{15}$$

where $u_i = \vec{u}(\vec{x}_i) \cdot \vec{n}_i$, $\vec{r}_i = \vec{x}_i - \vec{x}_0$, $\vec{x}_i$ is the midpoint of edge γ_i and l_i is its length (see Fig. 4(b)). $|\Omega|$ denotes the area of the polygon. The last equation defines a method for vector reconstruction at an interior point of the polygon, which we will denote as Perot's method using 6 edges (PE6), as it is usually applied to hexagonal shaped polygons.

In Perot's analysis, $\vec{u}$ is assumed to be a constant vector field, what readily ensures that the method is at least first order accurate. Moreover, the scheme is also exact for linear fields on aligned polygons, as shown in Appendix A, leading to second order in this case.

In order to extend the method to the sphere, we locally project the polygon onto the tangent plane at the point we want to reconstruct the vector field. The normal components of the vector field at the edges midpoints are projected as well, preserving the normal fluxes (this is done as described in [13]). Perot's planar method is then used to obtain the vector field at the point of tangency. In this way, the accuracy of the reconstruction will be given by the order of the planar reconstruction (generally first order, with second order on aligned polygons).

Alternatively, it is possible to use the geodesic area and lengths of the polygon in expression (15), employing the vectors $\vec{r}_i$ expressed directly in Cartesian coordinates in $\mathbb{R}^3$. The resulting vector is then projected onto the tangent plane to the sphere. Although these two approaches are not equivalent, they lead to very similar results.

b) Reconstruction using tangent vectors

Perot developed a similar reconstruction method when the tangential components of a planar vector field are known at the edge midpoints. In this case, the reconstructed vector is approximated as

$$\vec{u}_0 = \frac{1}{|\Omega|} \vec{k} \times \sum_{i=1}^{n} \vec{r}_i u_i l_i, \tag{16}$$

where l_i is the length of γ_i and $\vec{r}_i = \vec{x}_i - \vec{x}_0$. The reconstructed vector field represents exactly constant planar vector fields and, if $\vec{x}_0$ is the centroid of Ω and the polygon is aligned, also represents exactly linear vector fields. The extension of this reconstruction to the sphere is done as for Perot's scheme based on normal vector components.

In Voronoi C grids, this method can be used in a similar way as described for the method based on Whitney elements, considering the normal components of the Voronoi cells as the tangent components of the triangular cells. Thus, the method is applied for triangular cells and will be denoted as PE3 method.

2.5. Polynomial reconstruction

We now describe a local linear reconstruction using a least square fit, which has been considered in [8] for planar triangles. We show how to extend the scheme to planar and spherical polygons.

Let $\vec{u}$ be a linear vector field on the plane of the form

$$\vec{u}(\vec{x}) = \vec{a}_0 + A\vec{x} = \vec{a}_0 + \vec{a}_1 x + \vec{a}_2 y, \tag{17}$$

where $\vec{x} = (x, y)$, $\vec{a}_0 = (a_0^x, a_0^y)$ and

$$A = [\, \vec{a}_1 \quad \vec{a}_2 \,] = \begin{bmatrix} a_1^x & a_2^x \\ a_1^y & a_2^y \end{bmatrix}. \tag{18}$$

Assuming that the normal edge components (u_i) of a set of k edges are known at the edge midpoints, $\vec{x}_i = (x_i, y_i)$, then the least square problem may be stated as finding $\vec{a} = [a_0^x, a_0^y, a_1^x, a_1^y, a_2^x, a_2^y]$ that satisfies

$$\vec{u}(\vec{x}_i) \cdot \vec{n}_i = \vec{a}_0 \cdot \vec{n}_i + (A\vec{x}_i) \cdot \vec{n}_i = u_i, \quad i = 1, ..., k, \tag{19}$$

where n_i^x and n_i^y are respectively the first (x) and second (y) components of the ith normal vector $\vec{n}_i$. In a matrix form the problem may be written as $M\vec{a} = \vec{b}$, where $\vec{b} = [u_1, ..., u_n]$, and

$$M = \begin{bmatrix} n_1^x & n_1^y & n_1^x x_1 & n_1^y x_1 & n_1^x y_1 & n_1^y y_1 \\ n_2^x & n_2^y & n_2^x x_2 & n_2^y x_2 & n_2^x y_2 & n_2^y y_2 \\ \vdots & \vdots & \vdots & \vdots & \vdots & \vdots \\ n_k^x & n_k^y & n_k^x x_k & n_k^y x_k & n_k^x y_k & n_k^y y_k \end{bmatrix} \tag{20}$$

For the problem to be interpolatory, only 6 edges would be needed to recover a linear vector field, as we have 6 unknowns $(\vec{a})$. In this case, a hexagon would have the right number of degrees of freedom to solve the interpolatory problem. However, for pentagons or regular hexagons M has rank 5, and more edges need to be considered. To reconstruct the vector field at a node (triangle vertex), or Voronoi cell centroid, we use 2 levels of neighbours, to preserve symmetry,
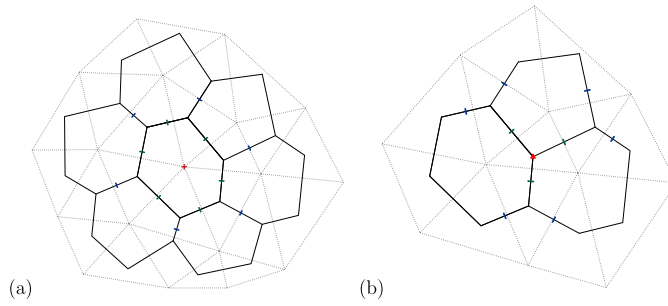
Fig. 5. Examples of stencils used for reconstructions. Line marks indicate the edge midpoints, where the normal components are know. On the left, the set of points centered at Voronoi polygon, on the right, centered at a triangle.

resulting in 12 edges for the hexagon (see Fig. 5(a)) and 10 edges for the pentagons. We denote this approach as LS12. If the reconstruction is required for a triangle circumcenter, or triangle barycentre, then a 9 point stencil (shown in Fig. 5(b)) may be used. This scheme is denoted as LS9.

For the spherical case, we use a similar technique to that used in [30], where a local orthogonal projection to a tangent plane at the reconstruction point is made. The implementation is done considering a rotation of a certain neighbourhood of nodes around a cell node or triangle circumcenter (as shown in Fig. 5) to the north pole, which in Cartesian coordinates will be assumed as $(0, 0, 1)$. The orthogonal projection is obtained simply ignoring the z coordinates of the nodes. The planar method is then applied, and the computed reconstructed vector is rotated back to the original point.

The polynomial vector reconstruction requires the solution of a least squares problem, which can turn out to be expensive when compared to other methods. In our implementation, we use a QR decomposition at each reconstruction as described in [31]. This is a robust method, reasonably fast and stable. It is possible to precompute and store the pseudo inverse of M (given by $(M^t M)^{-1} M^t$), as it only depends on grid structures. This largely reduces the computational time at a cost of considerably more memory usage. If the reconstruction is required only for the cell nodes or triangle circumcenters, and these points are chosen to be the origin of the local coordinates systems, only the first two lines of the pseudo inverses of M need to be stored. The system is weighted in order to keep linear and constant terms with the same order of magnitude (as done in [30]), improving numerical stability.

2.6. Radial basis functions

A radial basis function (RBF) [32,14] depends only on the distance from the point where it is computed to its center. Methods based on RBFs are easily applied on the sphere [33,34] and are suited for local vector field reconstructions as described in [9,35,36]. RBFs have been recently used with success for vector reconstruction on atmospheric models using non structured grids [37,1].

Consider k radial basis functions ϕ_i, relative to a local set of edges of the grid, each centered at an edge midpoint $(\vec{x}_i)$, of the form

$$\phi_i(\vec{x}) = \phi\big(d(\vec{x}, \vec{x}_i)\big), \tag{21}$$

where $d(\cdot, \cdot)$ is chosen as the geodesic distance on the sphere and ϕ is a positive kernel to be chosen in the sequence. The reconstructed vector field will be expressed as

$$\vec{u}(\vec{x}) = \sum_{i=1}^{k} \lambda_i \phi_i(\vec{x}) \vec{n}_i, \tag{22}$$

where $\vec{n}_i$ are the edge normal unit vectors and λ_i will be determined as the solution of

$$\sum_{i=1}^{k} \lambda_i \phi_i(\vec{x}_j) \vec{n}_i \cdot \vec{n}_j = u_j, \quad j = 1, ..., k, \tag{23}$$

where u_j are the normal vector components given at the edge midpoints. Problem (23) is a linear system of equations with coefficients $a_{ij} = \phi(d(\vec{x}_j, \vec{x}_i)) \vec{n}_i \cdot \vec{n}_j$. The resulting matrix is symmetric and, depending on the radial function, positive definite (see [32]). This is the case with the positive definite Gaussian kernel,

$$\phi(r) = e^{-(\epsilon r)^2}, \tag{24}$$

where ϵ is a shape parameter.

The parameter ϵ has to be chosen properly, since it is related to a duality between precision and stability [38,14]. If ϵ is too large, the (relevant) support of the radial basis function will be too small, very close to each edge point. As a result, the

matrix will be very well conditioned (almost diagonal), but the reconstruction may have poor accuracy. If ϵ is small enough such that every node contributes in the other nodes reconstruction, but still large enough so that the system is numerically stable, then normally a good precision is obtained. If the shape parameter was zero, the matrix would be formed only by ones and the problem would be ill posed. For a fixed ϵ, the scheme will be asymptotically unstable for very fine grids, since $d(\vec{x}_j, \vec{x}_i)$ would tend to zero, and the matrix entrances would all tend to one.

Ruppert [35] analysed the use of RBFs on staggered grids and concluded that an optimal shape parameter for the Gaussian kernel is $\epsilon = 2$ for a Rossby–Haurwitz wave number 4. The ICON shallow water model [37] employs a constant shape parameter (between 1 and 2) for the Gaussian kernel. Our experiments indicate that fixed shape parameters are adequate for the grid resolutions in use nowadays, leading to converging schemes, although with fast growing condition numbers for finer grids.

If ϵ is taken to be dependent on grid resolution (e.g. $\epsilon = C/h$, with C constant and h the mean grid length), then the matrix remains well conditioned for any grid refinement. However, the precision would be also almost independent of the grid level, with no convergence to be expected for fine grids. Rosatti et al. [39] used a shape parameter depending on the grid resolution ($\epsilon = 4/h$) with the addition of a linear polynomial part to a (multiquadric) RBF basis in order to ensure convergence. The addition of a polynomial part to the RBF basis is particularly important when using conditionally positive definite kernels, which otherwise may lead to a singular system (cf. [32]). With the positive definite Gaussian kernel employed here, this is not necessary. However, the addition of a polynomial part may be quite beneficial, improving the approximations and helping to maintain convergence with ϵ dependent on the resolution. This will be shown in our experiments with the addition of a constant part to the Gaussian basis. Details about how to implement it are given in Appendix B.

We point out that our choice of RBF methods has been guided by the most popular schemes being used in global weather and climate models, also aiming to achieve computational efficiency. There are other interesting possibilities, such as exploiting non diagonal kernels for vector reconstructions, as suggested in [40], which are not considered here. The ill conditioning of the RBF methods could be an issue on very fine grids. Besides that, one may also have to deal with some kind of Runge phenomenon [41]. On the other hand, besides the addition of a polynomial part to the RBF basis, it would still be possible to resort to stabilized linear system solvers (RBF-QR) or pre-conditioners [32,42,43], paying the price of higher computational costs.

In our implementation, we employ an LDL^t Cholesky decomposition of the system matrix, where L is unitary triangular and D diagonal. This decomposition is also exploited in the solution of the augmented system, resulting from the addition of a constant part to the RBF basis, as described in Appendix B. As the matrices depend only on the grid, the decomposition was precomputed and stored for later use in the vector reconstruction steps. We used three different sets of points to evaluate the RBF reconstruction (see Fig. 5):

- RB3 – Vector reconstruction to triangle circumcenter (VRTC) considering the 3 nearest edges to the circumcenter (Fig. 5(b) using only nearest neighbours),
- RB6 – Vector reconstruction to triangle vertex (VRTV) considering the 5 or 6 nearest edges to vertices (Fig. 5(a) using only nearest neighbours),
- RB9 – Vector reconstruction to triangle circumcenter (VRTC) considering the 9 nearest edges to the circumcenter (Fig. 5(b) using two level of neighbours).

2.7. Numerical experiments

Choice of grids and test case

The spherical grids used to analyse the reconstruction methods are the basic icosahedral grids, as described in [13] (see also Miura and Kimoto [44]). The construction of the grid starts by positioning the icosahedral with one vertex at each pole, and the others consequently lying on latitudes $\pm \arctan(0.5)$. We denote the basic icosahedral grid (with 12 nodes) as the 0-th grid level. Finer grids are obtained by recursively adding nodes at the midpoints of the edges and projecting them to the sphere. Each grid refinement level has approximately 4 times more triangles and half mean distance between nodes (triangle vertices) than the previous one.

The grid forms a Delaunay triangulation and the triangle vertices may be assumed as nodes for a Voronoi tessellation. The Voronoi polygons are constructed by connecting the circumcenters of the triangles around a node. The resulting Voronoi tessellation is composed of 12 regular pentagons and all other cells are hexagons. The Voronoi cells will be considered as computational cells.

As a test function for the vector reconstructions we employ a wave number $m = 8$ static Rossby–Haurwitz vector field. It is given in spherical coordinates as

$$u = a\omega_0 \cos(\theta) + a\omega_m \cos^{m-1}(\theta)\big(m\sin^2(\theta) - \cos^2(\theta)\big)\cos(m\lambda),$$
$$v = -am\omega_m \cos^{m-1}(\theta)\sin(\theta)\sin(m\lambda), \tag{25}$$

where $\theta \in [-\pi/2, \pi/2]$ is the latitude, $\lambda \in [-\pi, \pi]$ is the longitude, u and v are respectively the zonal and meridional winds, and the parameters are as in [45]: $a = 6.37122 \times 10^6$, $\omega_m = \omega_0 = 50 ms^{-1}/a = 7.848 \times 10^{-6}$.
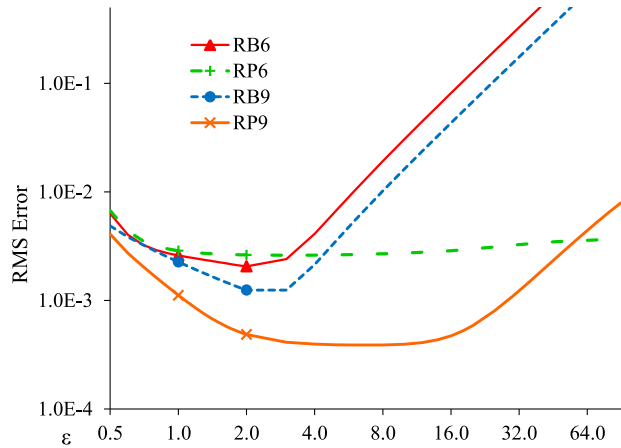
Fig. 6. Root mean square errors attained with different RBF schemes and their dependence on the shape parameter ϵ on a level 8 icosahedral grid.

Global errors at a set of n points are evaluated with the maximum norm and with the root mean square (RMS) (or mean quadratic) norm, given respectively by

$$E_{max} = \max_{i=1,\dots,n} \|\mathbf{v}_i - \tilde{\mathbf{v}}_i\|, \tag{26}$$

$$E_2 = \sqrt{\frac{\sum_{i=1}^{n} \|\mathbf{v}_i - \tilde{\mathbf{v}}_i\|^2}{n}}, \tag{27}$$

where $\mathbf{v}_i$ is the exact scalar or vector value, $\tilde{\mathbf{v}}_i$ the approximated value at each point i and $\|\cdot\|$ is the Euclidean norm.

To evaluate the reconstruction at general points we consider a remapping to a uniformly spaced longitude–latitude grid (with $0.25°$ spacing).

Results

We start this section investigating the effects of the variation of the shape parameter within the RBF methods. In Fig. 6 we display the RMS errors (on grid level 8) for vector reconstructions of the Rossby–Haurwitz wave with the radial basis function methods centered on Voronoi cells (RB6) and on triangles (RB9) (according to Fig. 5(a) and Fig. 5(b) respectively). We also tested both schemes with the addition of a constant part to the RBF basis (the resulting methods are denoted RP6 and RP9). We can observe that the schemes RB6 and RB9 lead to optimal results with ϵ around 2. For larger values of ϵ the precision deteriorates. The addition of the constant part has the effect that the scheme RP6 maintains practically the same accuracy achieved with $\epsilon = 2$ for much larger values of the shape parameter. With the larger stencil, used by RB9 and RP9, the extra constant part improves the precision of the method and broadens the range of ϵ for which the best results are obtained, making RP9 more robust than RB9. These effects are particularly interesting when considering the use of variable shape parameters. We have tested the methods with $\epsilon = \epsilon_0/h$, with ϵ_0 chosen such that $\epsilon = 2$ for grid level 5. With this choice of ϵ the related matrices remain all well conditioned, with limited condition numbers. We observe in Fig. 7 that with RB6 and RB9 the errors do not decrease from level 6 on (the same kind of behaviour has been observed in [35]). With the constant part added, schemes RP6 and RP9 maintain convergence up to level 9 (where $\epsilon = 32$). However, the convergence order of RP9 deteriorates, tending to first order on finer levels (which would be the convergence order of constant approximations). The same effect should eventually occur with RP6 at finer grid levels, although second order is attained until level 9. From a practical point of view, one would rather employ the best parameter for each level, leading to a stable scheme with smaller errors. The addition of the constant part broadens the range of possible choices for the parameter ϵ. In our following experiments, restricted to grid levels up to 9, the choice of a fixed value of $\epsilon = 2$ is adequate for all cases.

In Fig. 8 we show the maximum and RMS errors of the vector reconstructions to triangle circumcenters (VRTC) and vertices (VRTV) of the Rossby–Haurwitz wave using the methods described so far, as well as for a hybrid method (HYB), to be introduced in the next section. Figs. 9, 10 and 11 show the error distributions with the different methods on a level 7 icosahedral grid.

The methods based only on the information of the 3 edges surrounding a triangle (Perot's PE3, Whitney's WT3, Radial Basis Function RB3) show similar errors, with only first order accuracy in both maximum and RMS errors. The error distributions are also very similar, all revealing a strong grid imprinting in both low frequency (coarse grid pattern) and high frequency (grid scale noise) (cf. Fig. 9).

Perot's (PE6) and Edge-Based Basis (EB6) methods defined for Voronoi cells present an approximate second order accuracy in the RMS error, but only first order accuracy in the maximum norm. This indicates that at some locations the
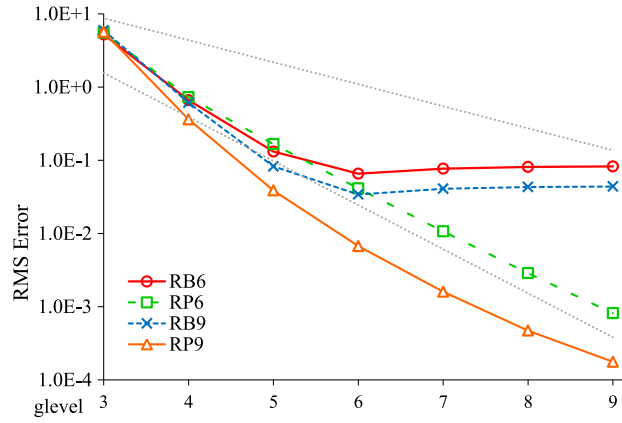
Fig. 7. Root mean square errors attained with different RBF schemes on several icosahedral grid levels, with shape parameters of the form $\epsilon = \epsilon_0/h$, where h is the average grid distance (in radians) of the corresponding grid. On grid level 5, $\epsilon = 2$.
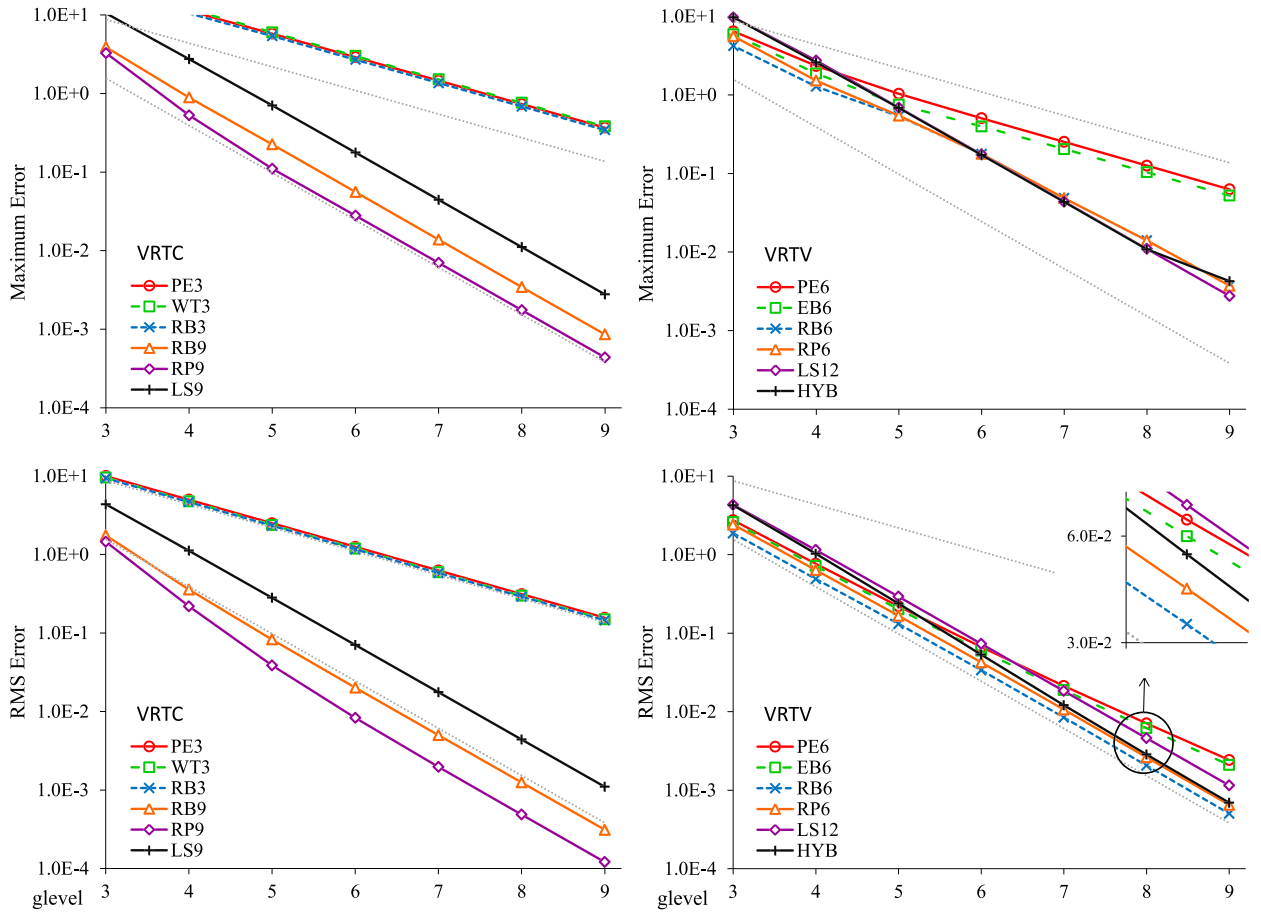
Fig. 8. Errors for the vector reconstructions to triangle circumcenters (left) and to triangle vertices (right) for the Rossby–Haurwitz wave vector field. On the top line the maximum errors are shown and, on the bottom line, the RMS errors. Dotted gray lines are references for first and second order convergence rates.

convergence is of first order, although in the average it is of second order. The places where higher errors are present reveal a strong coarse grid pattern (see Fig. 11).

The linear polynomial least square methods, centered at the Voronoi cells (LS12) and triangles (LS9) are second order accurate and have similar precision. With both methods, the error distribution for the remapping to a latitude–longitude grid shows a number 8 wave pattern, associated with the test function, and little grid imprinting.

(a) WT3 - Max= 1.35 RMS=1.4E-1   (b) PE3 - Max= 1.3 RMS=1.5E-1

(c) RB3 - Max= 1.2 RMS=1.35E-1
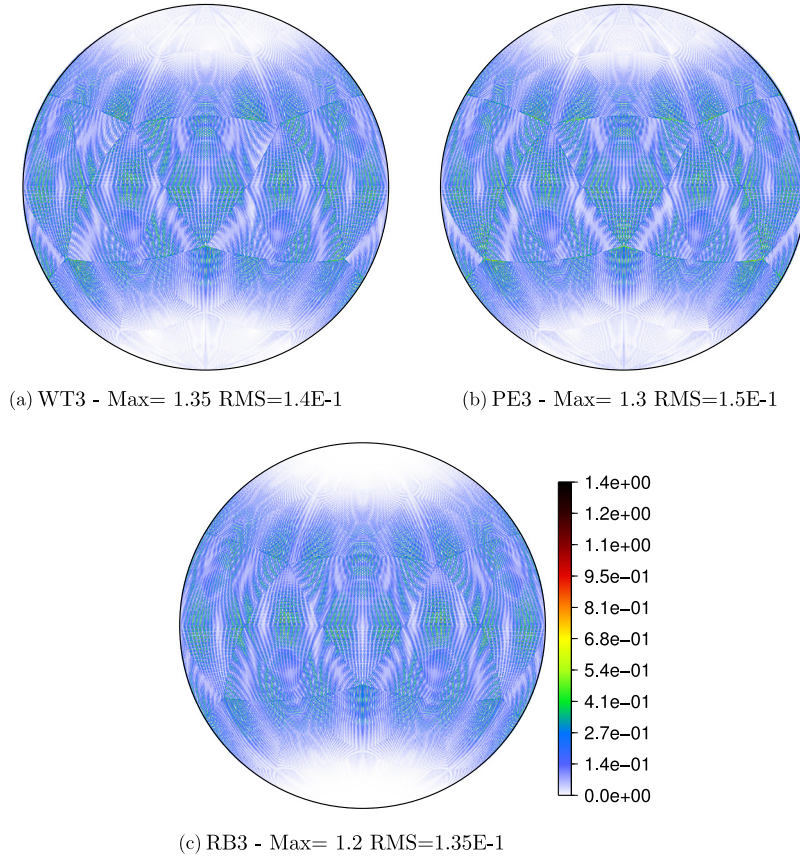
Fig. 9. Error distribution for the remapping of the Rossby–Haurwitz wave to a longitude–latitude grid ($0.25°$) using as vector reconstructions to the circumcenters of the triangles (VRTC): (a) Whitney basis (WT3), (b) Perot's method (PE3), (c) Radial Basis Function with 3 components (RB3). An icosahedral grid with level 7 was used in all cases. The maximum and RMS errors are indicated below each graph. (For interpretation of the colours in this figure, the reader is referred to the web version of this article.)

The Radial Basis Function method centered on Voronoi cells (RB6) shows approximately second order accuracy and a weaker coarse grid pattern in the error distribution. The version with an extra constant part (RP6) behaves very similarly, with slightly larger RMS errors, for this shape parameter $\epsilon = 2$ (we point out that in another test, with a rotational vector field, the errors with RP6 were smaller than with RB6). The RB9 method, centered at the triangles, is also of second order and more accurate than the RB6 method. Its variation including a constant part RP9 leads to even smaller errors, but with the same convergence order. The error distribution of both methods RB9 and RP9 are similar and present little grid imprinting. Overall, the RBF reconstructions perform comparatively well on these tests, with the versions employing the larger stencils leading to the smallest errors. For the range of grid levels tested, numerical instabilities were not present with $\epsilon = 2$. In Section 3.2 we will take the computational costs into account when comparing the different schemes.
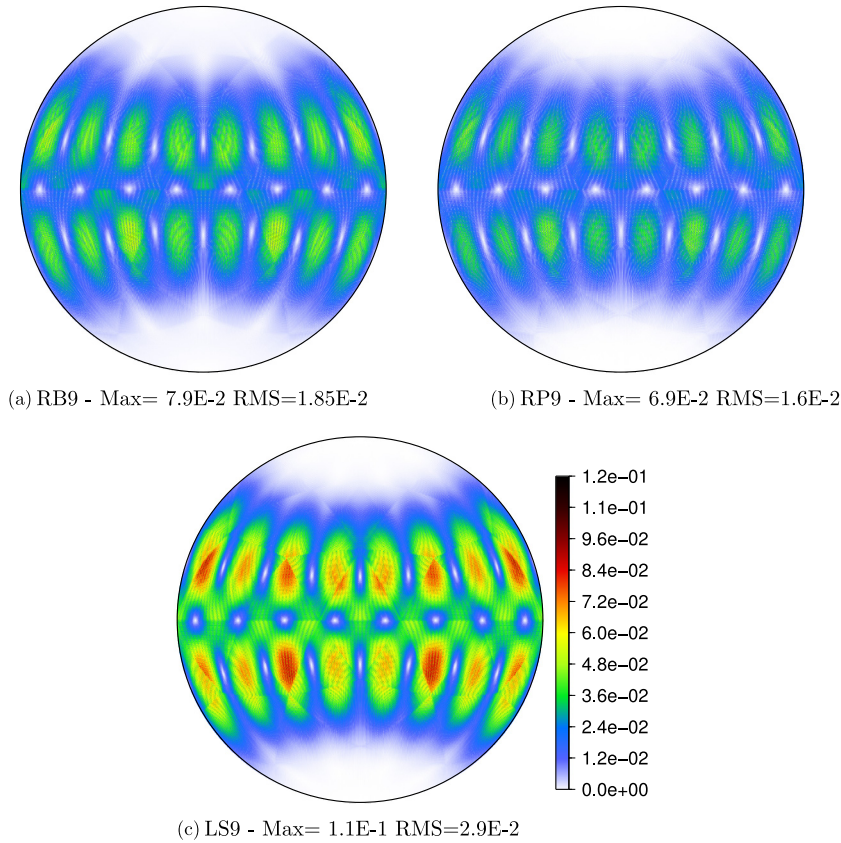
3. Hybrid vector reconstruction

3.1. On the icosahedral grid

The error distribution obtained with Perot's method (PE6) to triangle vertices presents a strong coarse grid pattern (see Fig. 11(b)). A similar error distribution is observed for the edge based basis method (EB6, cf. Fig. 11(a)). Both methods are generally only first order reconstructions. Second order error is attained on aligned cells as shown in Appendix A. Aligned cells are characterized by the alignment index (introduced in [13]):

$$\varXi(\Omega) = \frac{1}{n\bar{d}} \sum_{i=1}^{n/2} |d_{i+1+n/2,i} - d_{i+n/2,i+1}| + |d_{i+1,i} - d_{i+n/2+1,i+n/2}|, \qquad (28)$$

where $\bar{d} = \frac{1}{n}\sum_{i=1}^{n} d_{i,i+1}$, $d_{i,j}$ is the distance between polygon vertices $\vec{c}_i$, $i = 1, ..., n$, (we identify $\vec{c}_{n+1} = \vec{c}_1$). For the planar case $d_{i,j} = d(\vec{c}_i, \vec{c}_j) = \|\vec{c}_i - \vec{c}_j\|$ is the Euclidean distance between points $\vec{c}_i$ and $\vec{c}_j$, and on the sphere $d_{i,j} = d(\vec{c}_i, \vec{c}_j) = \arccos\langle \vec{c}_i, \vec{c}_j \rangle$ is the geodesic distance. The cell Ω is completely aligned if, and only if, $\varXi = 0$.

(a) RB9 - Max= 7.9E-2 RMS=1.85E-2   (b) RP9 - Max= 6.9E-2 RMS=1.6E-2

(c) LS9 - Max= 1.1E-1 RMS=2.9E-2

Fig. 10. Error distribution for the remapping of the Rossby–Haurwitz wave to a longitude–latitude grid (0.25°) using as vector reconstructions to the circumcenters of the triangles (VRTC): (a) Radial Basis Function with 9 components (RB9), (b) Radial Basis Function with 9 components with exact constant polynomial reproduction (RP9), (c) least squares reconstruction with 9 components (LS9). An icosahedral grid with level 7 was used in all cases. The maximum and RMS errors are indicated below each graph. (For interpretation of the colours in this figure, the reader is referred to the web version of this article.)

On icosahedral grids, there is an evident correlation between high alignment index values (badly aligned cells) and higher errors in both Perot's and EBBs reconstruction methods (see Fig. 12). This is explained in Appendix A for Perot's method. For the EBB method this is not so clear, but similar cancellation of first order error terms seems to take place on aligned cells.

Badly aligned cells (with $\varXi \geq 0.01$) are a minority in the icosahedral grid, explaining why these first order methods may show second order quadratic errors. We exploit this fact, proposing a hybrid method. We use Perot's method, a low cost scheme, on the majority of well aligned cells and a linear least square method only on badly aligned cells, which are cheaply identified by their alignment index. We have employed the hybrid method with a threshold value of 0.01 for the alignment index. For cells with alignment index smaller than 0.01 we used Perot's method (PE6) and the polynomial approximation with 12 edges (LS12) elsewhere. For a grid level 8, with this threshold value, approximately 8% of the cells are marked as badly aligned, and for a grid level 9, only 4%. The overall cost of the hybrid scheme is not much larger than the cost of Perot's method.

In Fig. 11(f) we show the error distribution for the reconstruction to triangle vertices (VRTV) followed by a remapping to a longitude–latitude grid using the a hybrid method. The grid pattern is largely reduced and the errors are similar to the ones obtained with the LS12 method. The overall precision improvement may be seen in Fig. 8, where we see that the error norms closely follow the LS12 curve.

One remark is due here: second order of Perot's method in aligned cells is ensured for cell centroids, which do not necessarily coincide with the triangle vertices on the icosahedral grid. Fortunately, on well aligned cells of the icosahedral grid, the centroids are closer to the triangle vertices (see Fig. 12(b)). Thus, an appropriate threshold choice for the alignment index captures both alignment and distance from cell centroid. We have also experimented reconstructions to the cell barycenter. In Fig. 13 we show the error distributions with Perot's method (PE6) and with the hybrid method. The improvements with the hybrid scheme are as before. We observe that it would be possible to replace the least square methods by RBF in the design of the hybrid scheme. We preferred the least square methods since they do not present ill conditioning problems.
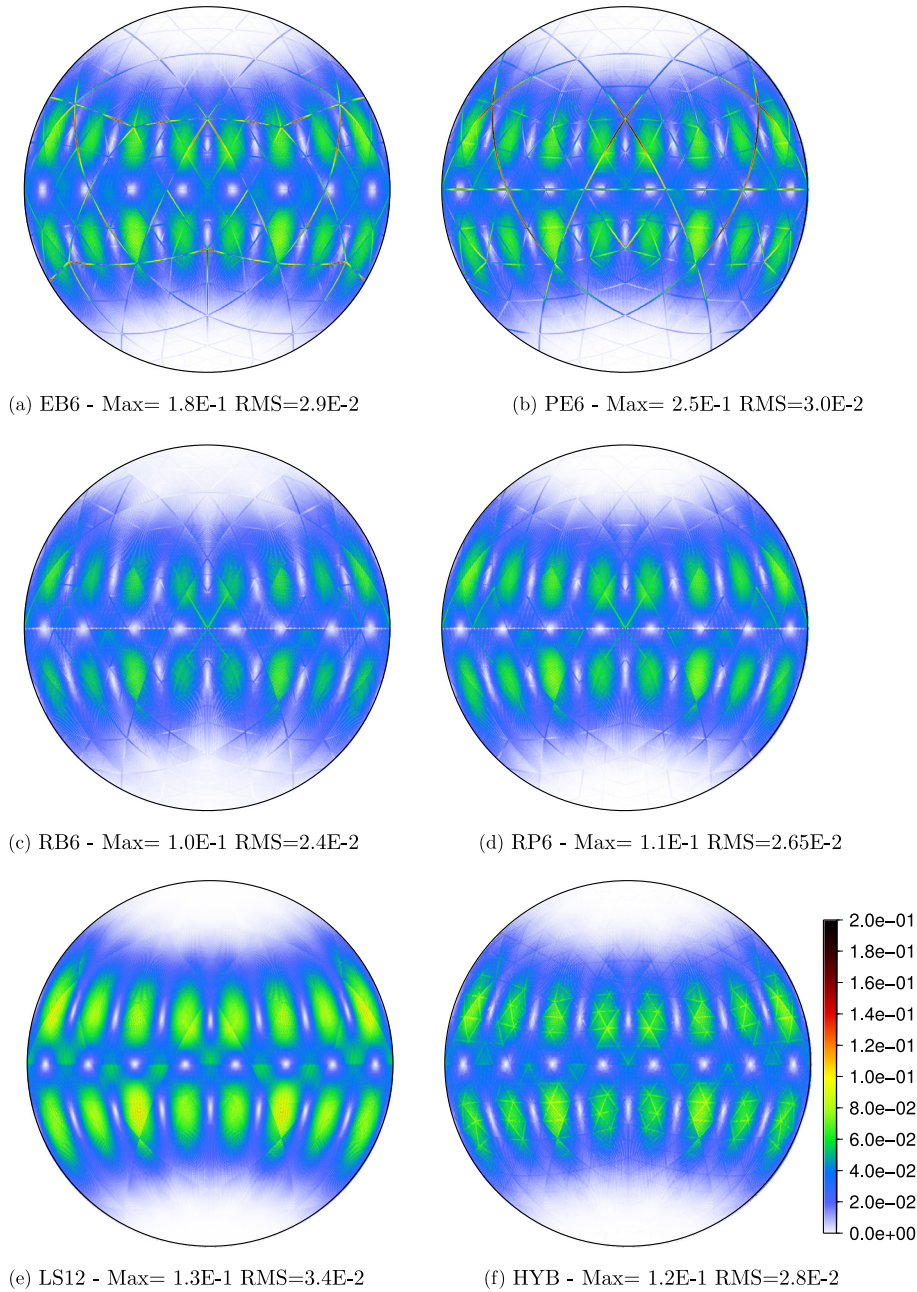
Fig. 11. Error distribution for the remapping of the Rossby–Haurwitz wave to a longitude–latitude grid (0.25°) using as vector reconstructions to the vertices of the triangles (VRTV): (a) Edge-based basis (EB6), (b) Perot's method (PE6), (c) Radial Basis Function with 6 (or 5) components (RB6), (d) least squares reconstruction with 12 (or 10) components (LS12), (e) Hybrid method (HYB). An icosahedral grid with level 7 was used in all cases. (For interpretation of the colours in this figure, the reader is referred to the web version of this article.)

3.2. Comparison of accuracy and costs of reconstruction methods

In Fig. 14 we compare the performance of the several methods concerning accuracy and computational efficiency. The experiment consists of two phases. First, a reconstruction of the vector field is carried out either to triangle circumcenters, with methods using the 9 points of Fig. 5(b), or to triangle vertices, with the schemes that employ the 6 or 12 points of Fig. 5(a). In the second step, we employ interpolation with barycentric Wachspress coordinates to remap the vector field to a uniform longitude–latitude grid. The points of the uniform grid will lie in arbitrary locations with respect to the cells of the icosahedral grid. For reconstructions to triangle circumcenters, the RBF methods presented better results than the least square LS9 scheme, being cheaper and more precise. RP9 was the most accurate scheme, but more expensive than RB9.
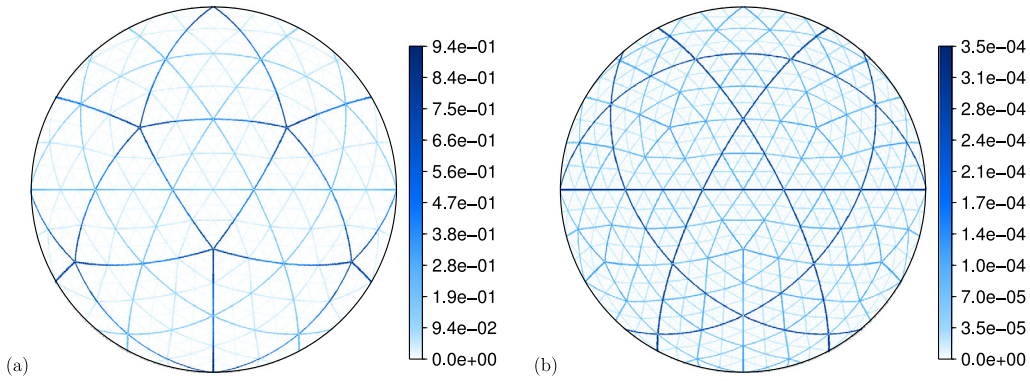
Fig. 12. (a) Alignment index distribution and (b) distance from cell nodes (triangle vertices) to cells centroids for level 7 icosahedral grid. (For interpretation of the colours in this figure, the reader is referred to the web version of this article.)

(a) PE6 - Max= 9.7E-2 RMS=1.3E-2   (b) HYB - Max= 4.3E-2 RMS=1.2E-2
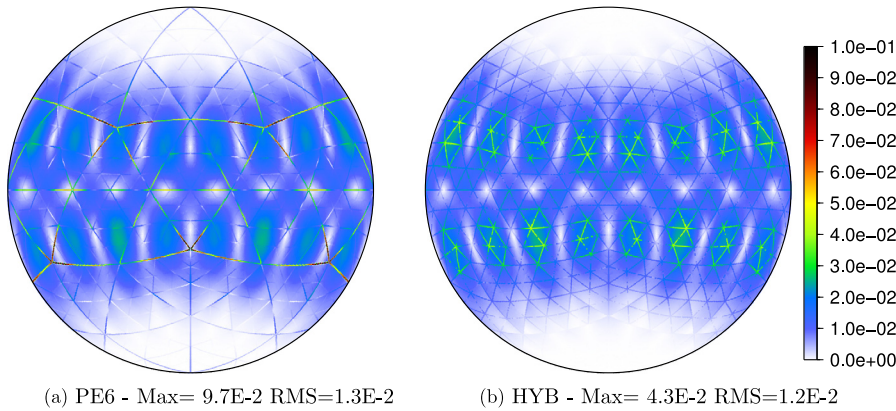
Fig. 13. Error distribution for the vector reconstruction to Voronoi cell centroids (VRVB) on a grid level 7 icosahedral grid using (a) Perot's method (PE6) and (b) hybrid method (HYB). For the hybrid scheme the alignment index threshold used was 0.01 (approximately 16% of the cells were considered non-aligned). (For interpretation of the colours in this figure, the reader is referred to the web version of this article.)

Among the schemes leading to vector values at the triangle vertices, RB6 and the hybrid scheme were the most effective, leading to smaller errors with low cost. The cheapest scheme was Perot's method, but it produced high maximum errors. Considering the results of the full remapping to a uniform grid we first observe that all RMS errors were of about the same order, the results ranging from 3.90E–03 with RP9 to 8.42E–03 with LS12. The variation in the maximum errors was larger, RP9 lead to a maximum error of 1.74E–02 and Perot's method PE6 was the less accurate scheme, with a maximum error of 1.23E–01. When the computational costs were taken into account, then again RB6 and the hybrid scheme were very competitive. The hybrid method was slightly less accurate than RB6 (maximum errors of 2.86E–02 and 2.49E–02 respectively), but about 20% faster. The hybrid method was ten times faster than RP9 and 8 times faster than RB9.

We point out that in our results the Cholesky decompositions of the interpolation matrices for the RBF methods were precomputed. This largely reduces the computational costs, at a price of high increase in memory consumption. For the polynomial least squares reconstructions, we solve the systems completely when required, consuming therefore more processing time, but with no increase in memory usage. It would have been possible to precompute the pseudo-inverses of the LSQ system matrices, thus reducing the computational costs, but with an extra amount of memory required. In the hybrid method, since the LSQ procedure is used in only a small percentage of the cells, the costs to solve the LSQ problems have relatively little impact in the overall processing time. The hybrid method requires no extra memory, showing an advantage over RBF methods in this aspect.

Methods centered at triangular cells, such as the RB9 and LS9, present higher computational processing times. This happens for two reasons: there are approximately twice as many triangles as nodes; and also, the Wachspress coordinates calculations on hexagons or pentagons are more expensive than on triangles (more areas need to be computed). Some preprocessing of areas could be done in order to reduce costs. One advantage of this approach is the simplicity to locate an interpolation point in the grid. On Voronoi cells, simple distance checks are enough to robustly determine to which Voronoi cell a point belongs. On the other hand, on triangular cells, the precise determination to which triangle a point belongs is more complicated and subject to numerical imprecisions.

A way to reduce the costs of RBF and LSQ methods centered at triangles, avoiding area calculations, is the direct use of the RBF reconstruction functions or the LSQ reconstructed polynomials at arbitrary locations, using precomputed inverse
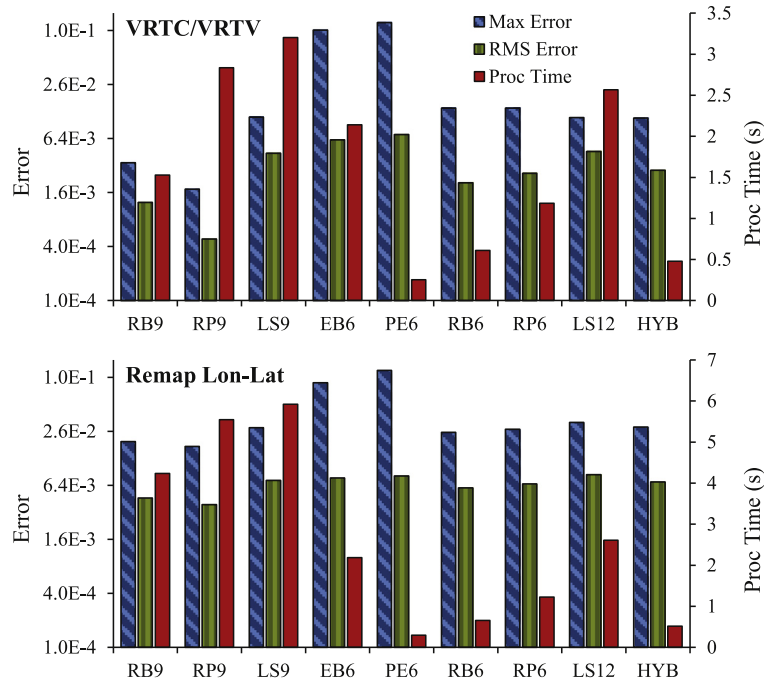
Fig. 14. Comparison of second order reconstructions methods concerning accuracy and computational costs. The figure on the top shows maximum and RMS errors for reconstructions to triangle circumcenters (VRTC) (for the 3 methods on the left) or to triangles vertices (VRTV) (for the other 6 schemes), with the corresponding computational costs. In the figure on the bottom we display the maximum and RMS errors for the full remapping to a longitude–latitude grid (0.25°). This remapping is done in two steps, first the reconstructions to either the triangle circumcenters or to triangles vertices (according to the schemes) are carried out. These are then followed by vector interpolations with Wachspress coordinates. The computational costs in the bottom figure comprise the two steps. The computational processing times are expressed in seconds and represent an average of 6 executions. The tests were done on a level 8 icosahedral grid.

or pseudo inverse matrices (here, the whole matrices need to be stored, not only 2 lines). This preserves the second order accuracy of the RB9 and LS9 method, but allows for discontinuities over the triangles edges. The same approach is possible with the LS12 and RB6 methods, again with discontinuities over the cell edges. The LS12 will be second order accurate, but the RB6 method will lead only to first order accuracy.

3.3. Reconstruction on spherical centroidal Voronoi tessellations

The hybrid scheme is applicable to other geodesic grids. In particular, we analysed it on Spherical Centroidal Voronoi Tessellations (SCVT), which are Voronoi diagrams in which the nodes are also the cell centroids. The SCVT grids may be thought as an optimization of the icosahedral grid [44], or as an arbitrary geodesic grid [4].
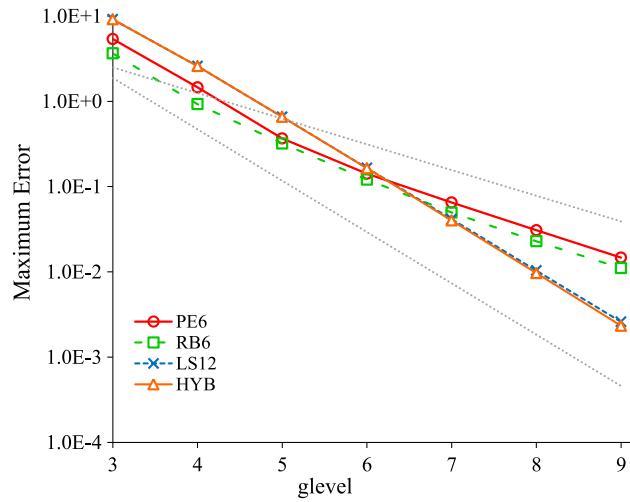
The icosahedral grid optimized with SCVT has been constructed as in [13], where the alignment properties of these grids were also investigated. We tested some of the reconstruction methods to triangle vertices, including the hybrid scheme, in the SCVT grids. In the hybrid method, we used the LS12 scheme on the 5% worse aligned cells for all grid levels. Fig. 15 shows maximum errors of the methods involved in the hybrid scheme (PE6, LS12, HYB) and of a radial basis function method (RB6). Both PE6 and RB6 methods lead to a first order approximation, while the least square and the hybrid scheme converge with second order.

Finally, we also tested the hybrid method on locally refined SCVT grids. We employed the density function described in [4] (Eq. (10.12)), where a region of radius approximately $\pi/6$ is refined with smooth transition to the rest of the sphere. We analysed the vector reconstruction to cell centroids using a Rossby–Haurwitz wave number 8 on this locally refined grid. In Fig. 16 we display the density distribution, showing the diameter of the cells (Fig. 16(a)). It is remarkable how the grid alignment index (Fig. 16(b)) captures the error pattern of Perot's method (Fig. 16(c)). The use of the hybrid scheme highly improves the results (Fig. 16(e) and Fig. 16(f)).

4. Vector reconstructions and semi-Lagrangian formulation

4.1. Formulation

In this section we consider which kind of requirements the vector reconstruction methods should fulfil, in order to be used in some traditional second order semi-Lagrangian schemes. We focus on two important points for semi-Lagrangian

Fig. 15. Maximum errors for the reconstruction to triangle vertices of the Rossby–Haurwitz wave number 8 on icosahedral grids optimized with SCVT. The dashed lines with no symbols indicate first and second order convergence references.

methods: the determination of departure points of particle trajectories and the approximation of fields at departure points. These aspects are relevant to a great number of semi-Lagrangian methods. One exception is McGregor's method, which does not employ interpolated values of the velocity field at arbitrary points [46]. (For this scheme the requirements would be different, involving accurate computation of derivatives of the wind field at grid point locations. We will not analyse this method here.)

The aspects we will consider can be dealt with in a simple passive advection method. This problem is closely related to tracer transport schemes on the sphere, an important aspect of atmospheric models.

The passive transport of a tracer substance ϕ obeys the equation

$$\frac{D\phi}{Dt} = 0 \tag{29}$$

where

$$\frac{D}{Dt} = \frac{\partial}{\partial t} + \vec{v} \cdot \nabla \tag{30}$$

is the Lagrangian or material derivative and $\vec{v}$ the fluid velocity. The fluid parcel trajectories $r(t)$ are such that

$$\vec{v}\big(t, r(t)\big) = \frac{dr(t)}{dt}. \tag{31}$$

In a semi-Lagrangian formulation, the tracer advection may be discretized as

$$\phi^{n+1} = \phi_*^n, \tag{32}$$

where the superscripts refer to time instants t_n and t_{n+1} ($t_{n+1} = t_n + \Delta t$) and the subscript $*$ denotes the departure point of Lagrangian trajectories arriving at the vertices of the triangulation.

We calculate the departure points as in [47]. The midpoint (r_m) of the trajectory ending at grid point r is approximated by the iterative procedure

$$r_m^{k+1} = \frac{r - \frac{\Delta t}{2} \vec{v}_m^k}{\|r - \frac{\Delta t}{2} \vec{v}_m^k\|}, \tag{33}$$

where k denotes the iteration step, $\vec{v}_m^k$ is the velocity at the intermediate time step $t_n + \Delta t/2$ at the trajectory midpoint r_m^k. The arrival point is used as the initial value r_m^0. Following the computation of r_m, the departure point is obtained as

$$r_* = 2\langle r_m, r \rangle r_m - r. \tag{34}$$

In this passive transport scheme, we will assume that the normal components of the velocity field at the cell edge midpoints of a Voronoi grid are known at any time instant. In order to obtain the velocities at trajectory midpoints, a vector reconstruction (to a general spatial location) will be required. If we keep the same proportion between the spatial and time spacings (a fixed CFL number) and the vector interpolation is second order accurate, then only 2 iterations in (33) will be sufficient to obtain third order accuracy in the departure point determination (as shown in Appendix C). If the vector
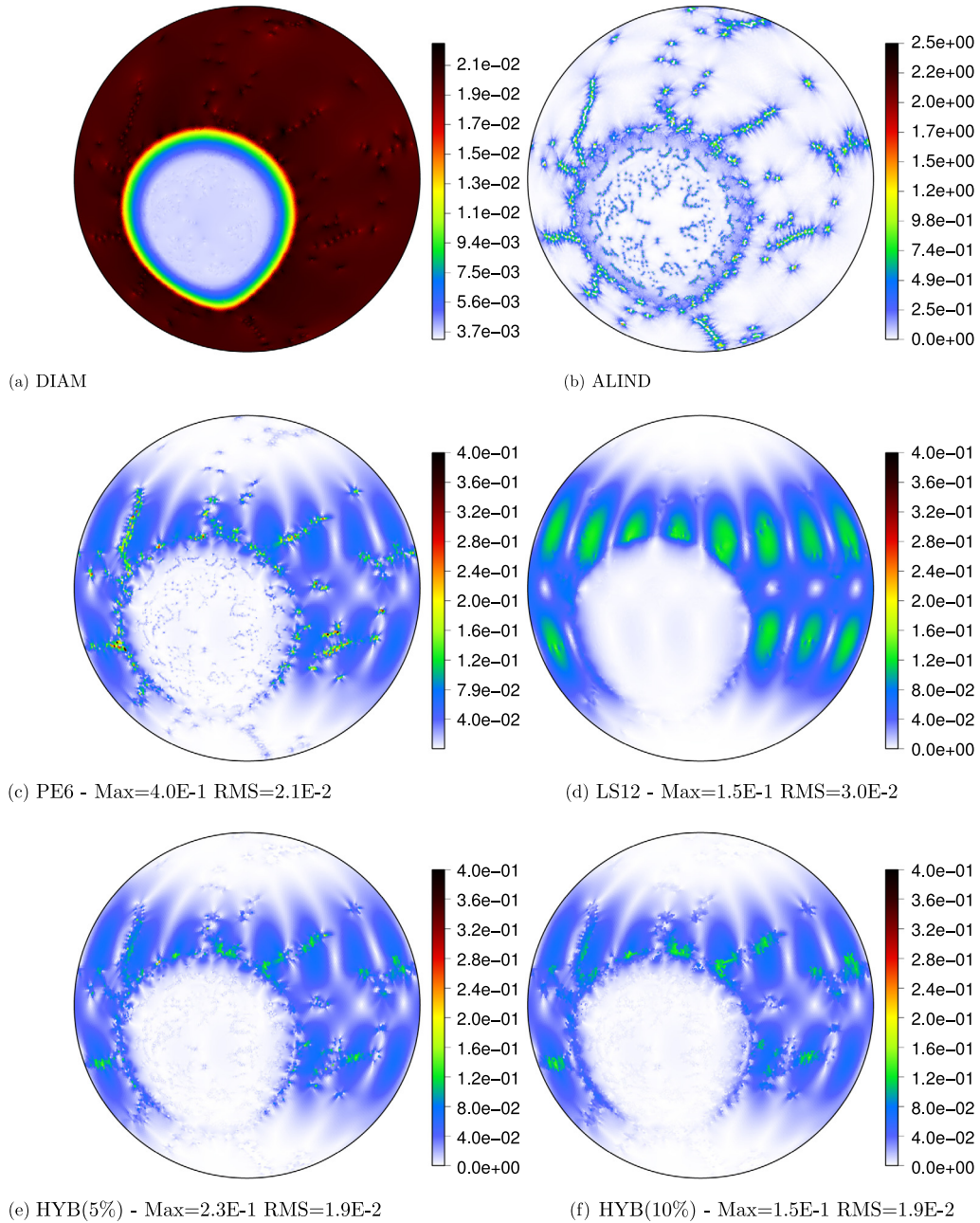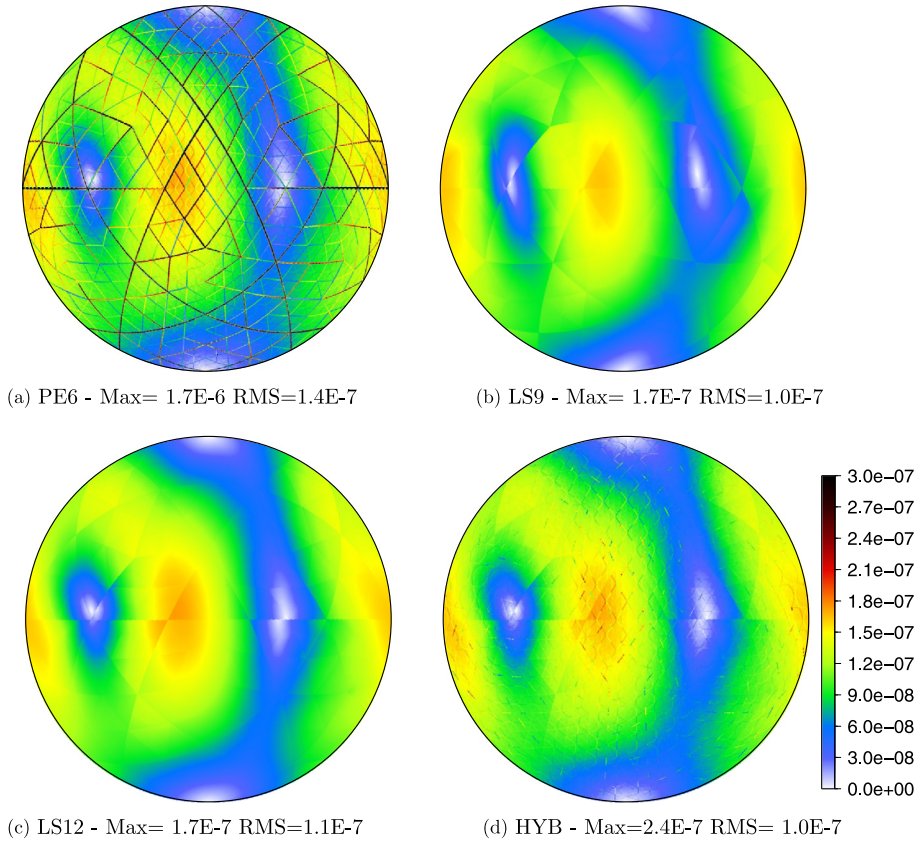
Fig. 16. Distributions for the (a) diameter of Voronoi cells, (b) alignment index, (c) error for Perot's method (PE6), (d) Least Squares method (LS12), (e) hybrid 95% PE6 and 5% LS12 method and (f) hybrid 90% PE6 and 10% LS12 method for reconstructions to cell centroids on a spherical centroidal Voronoi grid level 7, with local refinement. The maximum and RMS errors are indicated below each graph. (For interpretation of the colours in this figure, the reader is referred to the web version of this article.)

reconstruction method is only first order accurate, the departure point will be calculated with a second order error, even if more iterations are carried out. This makes clear the benefits of a second order accurate vector reconstruction in the trajectory computation.

Having the departure point with third order accuracy, the use of a third order method for the interpolations at the departure point locations, will lead to an overall third order accuracy per time step. The final error in the transported substance over a given period will be of second order, due to accumulation of errors in $O((\Delta t)^{-1})$ time steps (see Appendix C).

We have considered several third order schemes for scalar interpolation, including: Radial Basis Function methods [32,34, 14], polynomial Shepard's methods [48–52], Farin's C^1 method based on natural coordinates [53,54] and Renka's C^1 Hermite

(a) PE6 - Max= 1.7E-6 RMS=1.4E-7

(b) LS9 - Max= 1.7E-7 RMS=1.0E-7

(c) LS12 - Max= 1.7E-7 RMS=1.1E-7

(d) HYB - Max=2.4E-7 RMS= 1.0E-7

Fig. 17. Error on the evaluation of the departure points of the first time step (1/2048) of test case number 4 with reconstruction methods: (a) Perot (PE6), (b) least squares with 9 components (LS9), (c) least squares with 12 (or 10) components (LS12) and (d) Hybrid method (HYB). The colour black indicates an error greater or equal to $3.0e{-}7$. An icosahedral grid level 8 was used in all cases. The maximum and RMS errors are indicated below each graph. (For interpretation of the colours in this figure, the reader is referred to the web version of this article.)

interpolation [55]. The best results were obtained with Renka's C^1 method, which also presented lower computational costs. Therefore, it has been adopted as our standard scalar interpolation method.

4.2. Numerical experiments

Nair and Lauritzen [20] proposed a class of deformational test cases for transport methods on the sphere. To verify the properties of our semi-Lagrangian scheme we have chosen their test case number 4, which defines a non-divergent deformational flow with a zonal background velocity. The zonal (u) and meridional (v) components of the velocity field are given by

$$u(\lambda, \theta, t) = k \sin^2(\lambda' + \pi) \sin(2\theta) \cos(\pi t/T) + 2\pi \cos(\theta)/T,$$
$$v(\lambda, \theta, t) = k \sin(2(\lambda' + \pi)) \cos(\theta) \cos(\pi t/T),$$
(35)

where $\lambda' = \lambda - 2\pi t/T$, $\lambda \in [-\pi, \pi]$, $\theta \in [-\pi/2, \pi/2]$, $t \in [0, T]$. We adopt $k = 2$ and $T = 5$. The global maximum velocity of this vector field is about 2.9 radians per time unit (it was used in the evaluation of Courant numbers). The initial state of the tracer is chosen as two Gaussian distributions located at the equator, equidistant from Greenwich (see Fig. 19). These tests were defined in such a way that the final tracer distribution at instant T should coincide with the initial state, thus allowing exact computation of the numerical error at the end of the integration.

A semi-analytic expression for the trajectory calculation was derived in [20]. We have used it (with 100 sub time steps) to defined a reference trajectory, which was employed in the evaluation of the errors in the departure point estimates.

We first analysed the impact of the vector reconstruction on the departure point calculation. Figs. 17 and 18 show the distribution of the errors in the location of departure points in a given time step, with various reconstruction methods. We can clearly see coarser grid patterns where the errors of Perot's method are larger and how the hybrid method eliminates these larger errors by using the least square scheme at the appropriate locations. The error distributions with LS9 and LS12 are similar to the one obtained with the hybrid method. The results with the RBF schemes are of comparable quality (cf.
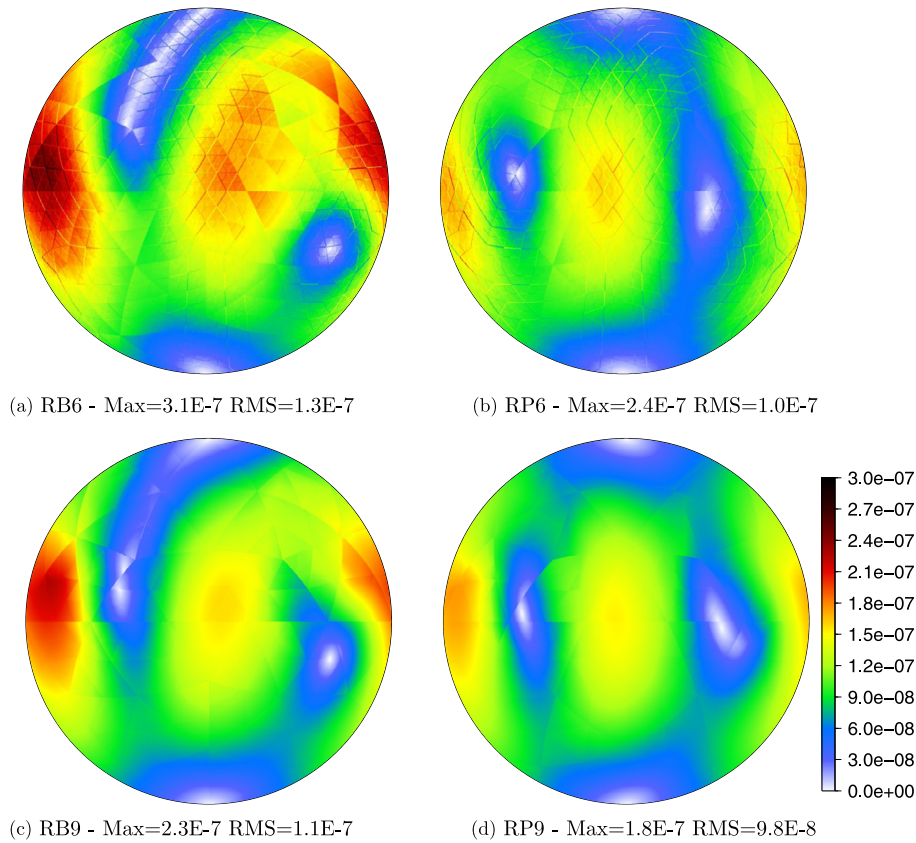
Fig. 18. Error on the evaluation of the departure points of the first time step (1/2048) of test case number 4 with reconstruction methods: (a) Radial Basis Function with 6 (or 5) components (RB6), (a) Radial Basis Function with 9 components (RB9), (c) RB6 with constant polynomial reproduction (RP6) and (d) RB9 with constant polynomial reproduction (RP9). The colour black indicates an error greater or equal to $3.0e$–7. An icosahedral grid level 8 was used in all cases. The maximum and RMS errors are indicated below each graph. (For interpretation of the colours in this figure, the reader is referred to the web version of this article.)

Fig. 18), with the addition of the constant part leading to some improvement, both in RP6 and RP9. All the RBF, LS and hybrid vector reconstructions are second order and adequate to be used in the trajectory computations.

In Fig. 19 we show the distribution of the tracer concentration at the initial time and at the instant of highest deformation (half of a full revolution cycle). In this test we have employed a grid level 7 and 512 time steps over the period $T = 5$ (corresponding to a CFL number around 3). The hybrid scheme was used in the trajectory computation and Renka's method was employed for the tracer interpolation.

The third order accuracy of the departure point calculation was verified numerically (see Fig. 20(a)), as well as the second order accuracy of the tracer concentration at the end of a full revolution (see Fig. 20(b)). We can notice that the use of relatively smaller time steps (lower Courant numbers) improves the precision in the departure points locations. On the other hand, the use of many time steps contributes to an increase in the accumulation of interpolation errors, since more time steps are employed. However, if the trajectory computation is too imprecise, this impacts the final error as well. In this example, a Courant number around 6 leads to smaller errors.

Renka's interpolation scheme is not monotonic and therefore, some spurious oscillations (and possibly negative concentrations) may appear, especially when the tracer concentrations present sharp gradients. To illustrate this, we have employed "slotted cylinders" as the initial state of the deformational test. Results for the tracer concentration at time $t = T/2$ are shown in Fig. 21 (top left). The final error at $t = T$ is displayed in the same figure (bottom left). We notice the occurrence of under- and over-shootings. We can enforce monotonicity forcing the interpolated values to lie between the maximum and minimum values given at the surrounding triangle vertices. The corresponding results for the deformational test with this monotone interpolation are in the right side of Fig. 21. We notice that the spurious oscillations disappear and that the slotted cylinder deformation is quite well captured at half time (compare with results given in [20]). Our semi-Lagrangian method is not inherently conservative, a property which may be desirable for tracer transport methods. It is relatively simple to employ fixers to make the scheme globally conservative. However, in order to ensure local conservation, the method would need to be modified, possibly along the lines of the CSLAM scheme proposed in [18].
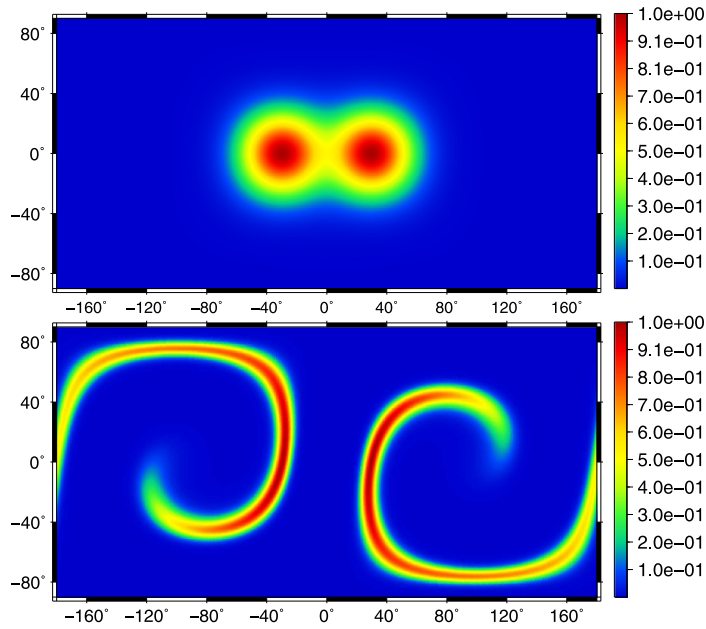
Fig. 19. Deformational flow test with zonal background flow (case number 4 of [20]) with Gaussian initial conditions for the mixing ratio ϕ. On the top, the initial condition is displayed. Bellow we have the numerical solution for ϕ at instant $t = T/2$ (after half of the integration time). A grid level 7 (cells with approximately 60 km diameters), $\Delta t = T/512$ (CFL number of approximately 3) and the hybrid vector reconstruction were employed. (For interpretation of the colours in this figure, the reader is referred to the web version of this article.)
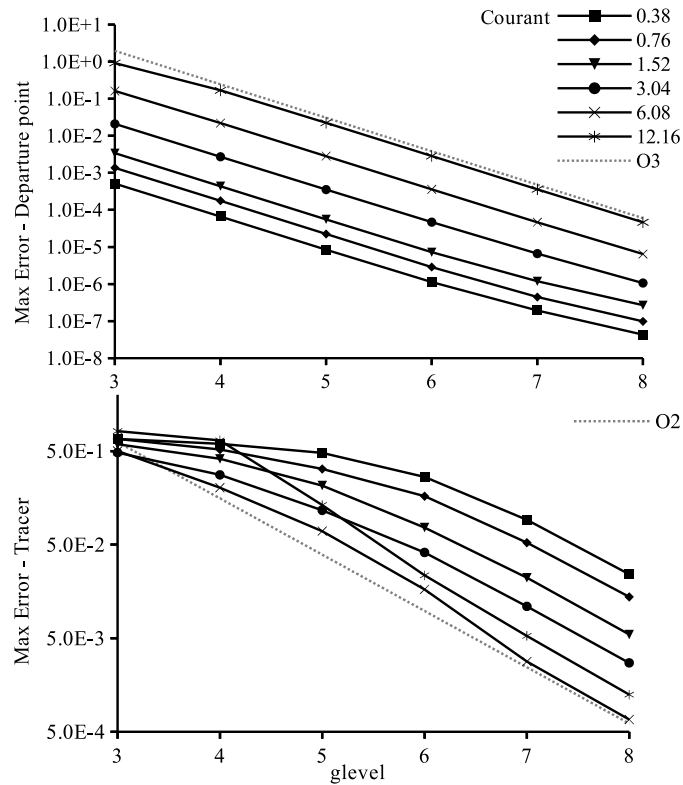
Fig. 20. Deformational flow test with zonal background flow (case number 4 of [20]) with Gaussian initial conditions for the tracer concentration ϕ. In the top graph, the maximum errors in the departure point locations (from all time steps) are displayed for different grid levels and CFL numbers. In all cases the hybrid reconstruction method was employed. In the bottom graph we have the corresponding maximum errors in the tracer ϕ after a full revolution ($t = T$). $O2$ and $O3$ are respectively second and third order convergence reference lines.
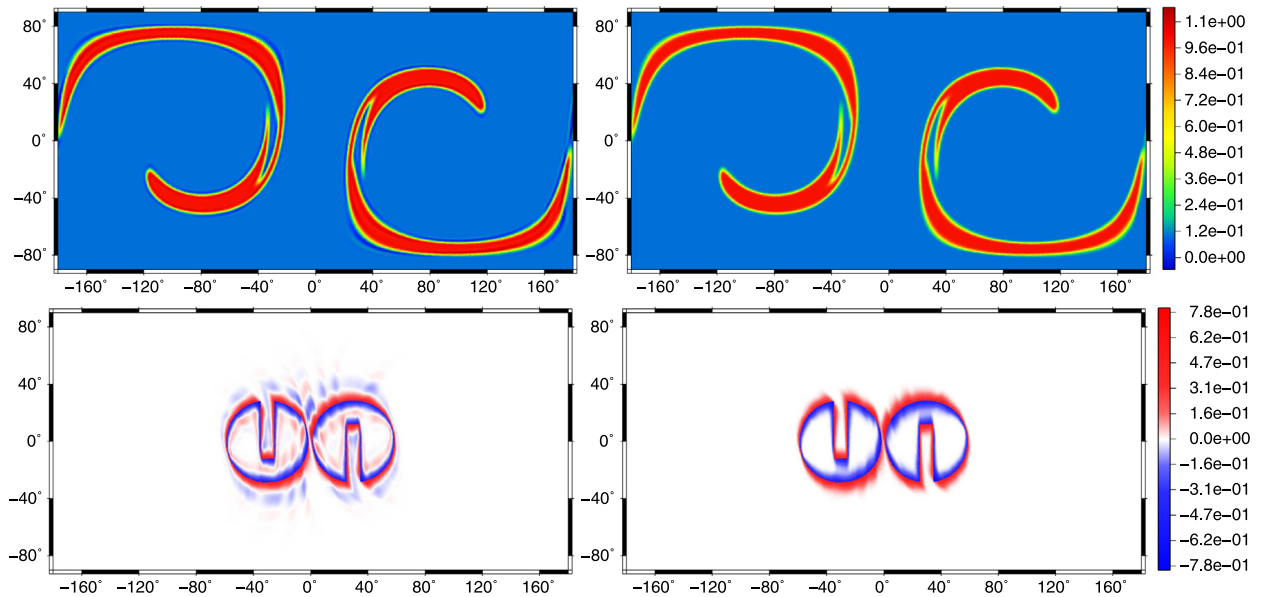
Fig. 21. Deformational flow test with zonal background flow (case number 4 of [20]) with slotted-cylinder initial conditions for the mixing ratio ϕ. On the top line, numerical solution for ϕ at time $t = T/2$ and, on bottom line, the error after a full revolution ($t = T$). On the left, no monotonicity was enforced. On the right, monotonicity was imposed. A grid level 7 (cells with approximately 60 km diameters) and 512 time steps were adopted (overall CFL number of approximately 3). (For interpretation of the colours in this figure, the reader is referred to the web version of this article.)

5. Concluding remarks

In this article we have shown how to employ several vector reconstruction methods on spherical polygonal C-grids, specially on Voronoi tessellations. We have compared edge-based finite element methods, Perot's method, least square reconstruction algorithms and Radial Basis Function schemes, also with the addition of a constant polynomial to the basis being considered. The emphasis was in reconstructing the vector field at any location on the sphere, as required in semi-Lagrangian transport methods. We reconstructed the fields to fixed locations (vertices, circumcenters or barycenters) and employed generalized barycentric coordinates to interpolate to desired locations. We derived a new hybrid scheme, combining Perot's method on well aligned grid cells (where it performs well) with least square approximations on the remaining cells. The resulting scheme is computationally efficient and leads to second order accuracy. It provides similar accuracy to least square and RBF reconstructions, with some computational advantages. The addition of a constant part to the RBF basis has been shown to be beneficial in some situations. These methods are adequate to be used within semi-Lagrangian trajectory computations (sufficiently accurate for second order methods), with the hybrid scheme and the RBF methods being more efficient in our implementation. We point out that if higher order in vector reconstructions is desired, the RBF or least square methods (with larger stencils) could be used, although the schemes would be less local and higher computational costs would be involved.

We remark that other schemes may be more interesting for specific purposes, as for example obtaining the tangential vector components, when the normal components are given. One may want, for instance, a scheme that maintains the geostrophic balance, as in [56], possibly with lower order accuracy, or that preserve some other mimetic properties. General methods, as studied here, may not be the best choice in specific cases, but provide applicable methods.

Acknowledgements

Appendix A. Accuracy of Perot's method on aligned polygons

In Perot's original work [7], the reconstruction method is built assuming a constant vector field, which ensures a first order approximation. Now, suppose that $\vec{x}_0$ is the center of mass of Ω and that $\vec{u}$ is linear, i.e. it may be written as $\vec{u} = \vec{u}_0 + D\vec{r}$, with D being a matrix with the constant derivatives of $\vec{u}$.

Parametrizing the edge of the polygon as $\gamma_i(s) = \vec{x}_i + s\vec{t}_i$, with $s \in [-l_i/2, l_i/2]$, Eq. (14) becomes

$$\int_{\Omega} \left(\vec{u} + \vec{r} \, \mathrm{div}(\vec{u}) \right) dA \;=\; \sum_{i=1}^{n} \int_{\gamma_i} \vec{r} \, (\vec{u} \cdot \vec{n}_i) \, dl$$

$$\Longleftrightarrow$$

$$\vec{u}_0 |\Omega| \;=\; \sum_{i=1}^{n} \int_{-l_i/2}^{l_i/2} (\vec{x}_i + s\vec{t}_i - \vec{x}_0) \left((\vec{u}_0 + D(\vec{x}_i + s\vec{t}_i - \vec{x}_0)) \cdot \vec{n}_i \right) dl$$

$$\Longleftrightarrow$$

$$\vec{u}_0 |\Omega| \;=\; \sum_{i=1}^{n} \int_{-l_i/2}^{l_i/2} (\vec{r}_i + s\vec{t}_i) \left((\vec{u}_0 + D\vec{r}_i) \cdot \vec{n}_i + (s D\vec{t}_i) \cdot \vec{n}_i \right) dl$$

$$\Longleftrightarrow$$

$$\vec{u}_0 \;=\; \frac{1}{|\Omega|} \sum_{i=1}^{n} \int_{-l_i/2}^{l_i/2} \left(\vec{r}_i u_i + s\vec{t}_i u_i + s\vec{r}_i (D\vec{t}_i \cdot \vec{n}_i) + s^2 \vec{t}_i (D\vec{t}_i \cdot \vec{n}_i) \right) dl$$

$$\Longleftrightarrow$$

$$\vec{u}_0 \;=\; \frac{1}{|\Omega|} \sum_{i=1}^{n} \vec{r}_i u_i l_i + \frac{1}{|\Omega|} \sum_{i=1}^{n} \vec{t}_i (D\vec{t}_i \cdot \vec{n}_i) \frac{l_i^3}{12}$$

where $\vec{r}_i = \vec{x}_i - \vec{x}_0$ and $u_i = \vec{u}(\vec{x}_i) \cdot \vec{n}_i = (\vec{u}_0 + D\vec{r}_i) \cdot \vec{n}_i$. Therefore, for a linear vector function the method is not exact, leading to a first order error term

$$E = \frac{1}{|\Omega|} \sum_{i=1}^{n} \vec{t}_i (D\vec{t}_i \cdot \vec{n}_i) \frac{l_i^3}{12}. \tag{A.1}$$

In summary, the reconstruction method is in general only first order accurate. Now, suppose that $\vec{x}_0$ is the center of mass and that Ω is an aligned polygon (see [13]), for which opposite edges are parallel and have the same length. In this case, $\vec{n}_i = -\vec{n}_{i+n/2}$, $\vec{t}_i = -\vec{t}_{i+n/2}$, $l_i = l_{i+n/2}$. It follows that the first order error term E vanishes:

$$E = \frac{1}{|\Omega|} \sum_{i=1}^{n} \vec{t}_i (D\vec{t}_i \cdot \vec{n}_i) \frac{l_i^3}{12}$$

$$= \frac{1}{|\Omega|} \sum_{i=1}^{n/2} \left(\vec{t}_i (D\vec{t}_i \cdot \vec{n}_i) \frac{l_i^3}{12} + \vec{t}_{i+n/2} (D\vec{t}_{i+n/2} \cdot \vec{n}_{i+n/2}) \frac{l_{i+n/2}^3}{12} \right)$$

$$= \frac{1}{|\Omega|} \sum_{i=1}^{n/2} \left(\vec{t}_i (D\vec{t}_i \cdot \vec{n}_i) \frac{l_i^3}{12} - \vec{t}_i (D\vec{t}_i \cdot \vec{n}_i) \frac{l_i^3}{12} \right) = 0.$$

As a consequence, Perot's method is second order accurate on aligned polygons, when the reconstruction is performed for the center of mass. The same result is valid on the sphere. The extension of this result to the sphere is done along the same lines used to show that the usual finite volume discretization of the divergence operator is of second order on spherical aligned polygons in [13]. Similar analysis also applies for the reconstruction method when the tangential components are known.

Appendix B. Solving RBF interpolation problems with a polynomial part

The interpolated vector field with the RBF basis including a polynomial term is given by

$$\vec{u}(\vec{x}) = \sum_{i=1}^{k} \lambda_i \phi_i(\vec{x}) \vec{n}_i + \sum_{i=1}^{d} \alpha_i \vec{p}_i(\vec{x}), \tag{B.1}$$

where the vector polynomials $(\vec{p}_i)$ form a basis of a d-dimensional vector polynomial space. The interpolation problem consists of finding the vectors $\vec{\lambda}$ and $\vec{\alpha}$ such that

$$\sum_{i=1}^{k} \lambda_i \phi_i(\vec{x}_j) \vec{n}_i \cdot \vec{n}_j + \sum_{i=1}^{d} \alpha_i \vec{p}_i(\vec{x}_j) \cdot \vec{n}_j = u_j, \quad j = 1, ..., k. \tag{B.2}$$

In order to complete the system, new conditions have to be included, since there are d extra unknowns. This is usually done (see [32]) by imposing that

$$\sum_{i=1}^{k} \lambda_i \vec{p}_j(\vec{x}_i) \cdot \vec{n}_i = 0, \quad j = 1, ..., d. \tag{B.3}$$

Defining the $k \times k$ matrix A, with $a_{ij} = \phi(d(\vec{x}_j, \vec{x}_i))\vec{n}_i \cdot \vec{n}_j$, and the $k \times d$ matrix B, with $b_{ij} = \vec{p}_j(\vec{x}_i) \cdot \vec{n}_i$, the resulting linear system is

$$\begin{bmatrix} A & B \\ B^t & 0 \end{bmatrix} \begin{bmatrix} \vec{\lambda} \\ \vec{\alpha} \end{bmatrix} = \begin{bmatrix} \vec{v} \\ 0 \end{bmatrix}, \tag{B.4}$$

where $\vec{v}$ is formed by the data $\{u_i\}_{i=1,k}$. The full matrix above is symmetric, but not positive definite, possessing no Cholesky decomposition. We point out that k must be larger than d, or else $\vec{\lambda} = 0$, and the non-linear RBF terms will not be part of the reconstructed field.

With the j-th column of B denoted by $\vec{b}_j$, the system may be written as

$$\begin{cases} A\vec{\lambda} + \sum_{j=1}^{d} \alpha_j \vec{b}_j = \vec{v} \\ \vec{b}_j \cdot \vec{\lambda} = 0 \quad (j = 1, ..., d) \end{cases} \tag{B.5}$$

Let

$$\vec{w}_v = A^{-1}\vec{v}, \tag{B.6}$$

and

$$\vec{w}_j = A^{-1}\vec{b}_j, \tag{B.7}$$

for $j = 1, ..., d$. It follows, after multiplying the first equation in (B.5) by A^{-1}, that

$$\vec{\lambda} = \vec{w}_v - \sum_{j=1}^{d} \alpha_j \vec{w}_j, \tag{B.8}$$

and, using that $\vec{b}_j \cdot \vec{\lambda} = 0$, $\vec{\alpha}$ may be obtained solving the $d \times d$ linear system $D\vec{\alpha} = d$, where

$$D_{ij} = \vec{b}_i \cdot \vec{w}_j = \vec{b}_i \cdot A^{-1}\vec{b}_j, \tag{B.9}$$

and

$$d_i = \vec{b}_i \cdot \vec{w}_v. \tag{B.10}$$

If the columns $\vec{b}_j$ are linearly independent, it follows that D is symmetric positive definite whenever A is. Once $\vec{\alpha}$ is obtained, $\vec{\lambda}$ is computed through Eq. (B.8).

This method requires the solution of $d + 1$ linear systems of dimension $k \times k$ to obtain $\vec{w}_v$ and $\vec{w}_j$ ($j = 1, ..., d$) (what is simple once the Cholesky decomposition of A is available), and the solution of a $d \times d$ system to obtain $\vec{\alpha}$. An alternative would be the direct use of the LU decomposition of the full matrix in system (B.4). This would be more efficient for larger values of k, but would require twice the memory for storing the LU decompositions.

For the constant polynomial reproduction, using the canonical basis for $\mathbb{R}^3$, the matrix B will have as rows the normal vectors relative to each data site edge. Therefore, $\vec{b}_j$ will be formed by the j-th components of the normal vectors. Since the normal vectors are not all coplanar (as they lie on different tangent planes to the sphere), the three $\vec{b}_j$ vectors are linearly independent and the problem is well posed for the Gaussian kernel as long as $k > 3$.

For linear reproduction, $d = 12$, and k must be greater than 12, leading to high computational costs. Therefore, we restricted our tests to the case of addition of a constant vector to the RBF basis.

Appendix C. Accuracy of the semi-Lagrangian scheme

We analyse here the influence of the number of iterations and of the vector interpolation order on the semi-Lagrangian scheme accuracy. Similar analysis (in one dimension) can be found in [57] and in [58], but not exactly as needed here. Our analysis is restricted to the $\mathbb{R}^2$ plane.
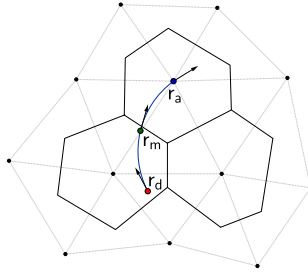
Fig. 22. Illustration of elements involved in the semi-Lagrangian trajectory calculation.

C.1. Departure point calculation with exact velocities

Define, for fixed $t \in [0, T]$,

$\mathbf{r}_d = \mathbf{r}(t)$, as the departure point;

$\mathbf{r}_m = \mathbf{r}(t + \Delta t/2)$, as the midpoint; and

$\mathbf{r}_a = \mathbf{r}(t + \Delta t)$, as the arrival point,

as in Fig. 22. Assuming regularity of $\mathbf{r}(t)$, we use its derivatives to define the velocity ($\mathbf{v}$), acceleration ($\mathbf{a}$) and jerk ($\mathbf{h}$), at the arrival, departure and midpoints.

Using Taylor expansions of $\mathbf{r}_a$ and $\mathbf{r}_d$ around $\mathbf{r}_m$ we obtain

$$\mathbf{r}_a = \mathbf{r}_m + \frac{\Delta t}{2}\mathbf{v}_m + \frac{\Delta t^2}{8}\mathbf{a}_m + \frac{\Delta t^3}{48}\mathbf{h}_m + O\left(\Delta t^4\right) \tag{C.1}$$

and

$$\mathbf{r}_d = \mathbf{r}_m - \frac{\Delta t}{2}\mathbf{v}_m + \frac{\Delta t^2}{8}\mathbf{a}_m - \frac{\Delta t^3}{48}\mathbf{h}_m + O\left(\Delta t^4\right). \tag{C.2}$$

Let

$$\tilde{\mathbf{r}}_m = \mathbf{r}_a - \frac{\Delta t}{2}\tilde{\mathbf{v}}_m, \tag{C.3}$$

be the final approximation to $\mathbf{r}_m$, with $\tilde{\mathbf{v}}_m$ being the corresponding final approximated velocity used to obtain $\tilde{\mathbf{r}}_m$. $\tilde{\mathbf{v}}_m$ is an approximation to the exact velocity $\mathbf{v}_m$ at the midpoint. Eq. (C.1) leads to

$$\tilde{\mathbf{r}}_m = \mathbf{r}_m + \frac{\Delta t}{2}(\mathbf{v}_m - \tilde{\mathbf{v}}_m) + \frac{\Delta t^2}{8}\mathbf{a}_m + \frac{\Delta t^3}{48}\mathbf{h}_m + O\left(\Delta t^4\right). \tag{C.4}$$

The departure point is estimated in the scheme as

$$\tilde{\mathbf{r}}_d = 2\tilde{\mathbf{r}}_m - \mathbf{r}_a = \tilde{\mathbf{r}}_m - \frac{\Delta t}{2}\tilde{\mathbf{v}}_m, \tag{C.5}$$

therefore,

$$\tilde{\mathbf{r}}_d = \mathbf{r}_m + \frac{\Delta t}{2}(\mathbf{v}_m - 2\tilde{\mathbf{v}}_m) + \frac{\Delta t^2}{8}\mathbf{a}_m + \frac{\Delta t^3}{48}\mathbf{h}_m + O\left(\Delta t^4\right). \tag{C.6}$$

Using Eq. (C.2), the error in the departure point calculation may be estimated as

$$\mathbf{e} = \tilde{\mathbf{r}}_d - \mathbf{r}_d = \Delta t(\mathbf{v}_m - \tilde{\mathbf{v}}_m) + \frac{\Delta t^3}{24}\mathbf{h}_m + O\left(\Delta t^4\right). \tag{C.7}$$

Thus, the accuracy of the trajectory, up to third order, depends on how well $\tilde{\mathbf{v}}_m$ approximates $\mathbf{v}_m$.

If the fluid velocity is known at any point in space and time, $\tilde{\mathbf{v}}_m$ depends only on the iterative process at instant $t_m = t + \Delta t/2$. With one iteration,

$$\tilde{\mathbf{v}}_m = \mathbf{v}(t_m, \mathbf{r}_a) = \mathbf{v}\left(t_m, \mathbf{r}_m + \frac{\Delta t}{2}\mathbf{v}_m + O\left(\Delta t^2\right)\right) = \mathbf{v}_m + O(\Delta t).$$

Eq. (C.7) now shows that we would have an error of $O(\Delta t^2)$ in the determination of $\mathbf{r}_m$.

If instead, two iterations are employed,

$$\tilde{\mathbf{v}}_m = \mathbf{v}\left(t_m, \mathbf{r}_a - \frac{\Delta t}{2}\mathbf{v}(t_m, \mathbf{r}_a)\right). \tag{C.8}$$

Using that

$$\mathbf{v}(t_m, \mathbf{r}_a) = \mathbf{v}(t + \Delta t/2, \mathbf{r}_a) = \mathbf{v}_a - \frac{\Delta t}{2}\mathbf{a}_a + O\left(\Delta t^2\right)$$

we obtain

$$\tilde{\mathbf{v}}_m = \mathbf{v}\left(t_m, \mathbf{r}_a - \frac{\Delta t}{2}\mathbf{v}_a + \frac{\Delta t^2}{4}\mathbf{a}_a + O\left(\Delta t^3\right)\right)$$

$$= \mathbf{v}\left(t_m, \mathbf{r}_m + \frac{\Delta t^2}{8}\mathbf{a}_a + O\left(\Delta t^3\right)\right) = \mathbf{v}_m + O\left(\Delta t^2\right),$$

since $\mathbf{r}_m = \mathbf{r}_a - \frac{\Delta t}{2}\mathbf{v}_a + \frac{\Delta t^2}{8}\mathbf{a}_a + O(\Delta t^3)$. It follows that in this case, $\mathbf{r}_m$ is obtained with an error of $O(\Delta t^3)$. More than two iterations will not improve this order of error.

C.2. Departure point calculation with approximated velocities

We can now discuss the impact of spatial errors in the evaluation of the velocity field at the trajectory midpoint. If we have an interpolation error of order $p \geq 1$ (assuming $\Delta x = \alpha \Delta t$) we obtain $\tilde{\mathbf{r}}_m = \mathbf{r}_m + O(\Delta t^{\min(p+1,3)})$ with two or more iterations. The midpoint and departure point of the trajectory will be third order accurate if at least two iterations are carried out and if the error in the velocity field spatial interpolation is at least two. The same conclusions apply for temporal errors in the approximation of the velocity values (for instance, a linear extrapolation of values at time t and $t - \Delta t$ is sufficient for providing second order in time).

Finally, we consider the errors in the transported quantity at the end of a given time interval. With a fixed relation $\Delta t = \alpha \Delta x$, the number of time steps necessary to reach a fixed instant is of the order of $(\Delta t)^{-1}$. If the errors per time step are of order p, they may accumulate along the $O((\Delta t)^{-1})$ time-steps, resulting in a final error of order $p - 1$. Therefore, if we want to guarantee a second order scheme we need: two iterations in the trajectory computations, a second order scheme for the vector reconstruction of the velocity field and a third order interpolation method for the transported scalar field.

References

[1] W.C. Skamarock, J.B. Klemp, M.G. Duda, L.D. Fowler, S.-H. Park, T.D. Ringler, A multiscale nonhydrostatic atmospheric model using centroidal Voronoi tessellations and C-grid staggering, Mon. Weather Rev. 140 (2012) 3090–3105.
[2] H. Wan, M.A. Giorgetta, G. Zängl, M. Restelli, D. Majewski, L. Bonaventura, K. Fröhlich, D. Reinert, P. Rípodas, L. Kornblueh, J. Förstner, The icon-1.2 hydrostatic atmospheric dynamical core on triangular grids part 1: Formulation and performance of the baseline version, Geosci. Model Dev. 6 (3) (2013) 735–763.
[3] A. Staniforth, J. Thuburn, Horizontal grids for global weather and climate prediction models: a review, Q. J. R. Meteorol. Soc. 138 (662) (2012) 1–26.
[4] L. Ju, T.D. Ringler, M. Gunzburger, Voronoi tessellations and their application to climate and global modeling, in: P. Lauritzen, C. Jablonowski, M. Taylor, R. Nair (Eds.), Numerical Techniques for Global Atmospheric Models, in: Lect. Notes Comput. Sci. Eng., vol. 80, Springer, Berlin, Heidelberg, 2011, pp. 313–342.
[5] B. Wang, G. Zhao, O. Fringer, Reconstruction of vector fields for semi-Lagrangian advection on unstructured, staggered grids, Ocean Model. 40 (1) (2011) 52–71.
[6] P. Raviart, J. Thomas, A mixed finite element method for 2-nd order elliptic problems, in: I. Galligani, E. Magenes (Eds.), Mathematical Aspects of Finite Element Methods, in: Lect. Notes Math., vol. 606, Springer, Berlin/Heidelberg, 1977, pp. 292–315.
[7] B. Perot, Conservation properties of unstructured staggered mesh schemes, J. Comput. Phys. 159 (1) (2000) 58–89.
[8] D. Vidovic, Polynomial reconstruction of staggered unstructured vector fields, Theor. Appl. Mech. 36 (2009) 85–99.
[9] L. Bonaventura, A. Iske, E. Miglio, Kernel-based vector field reconstruction in computational fluid dynamic models, Int. J. Numer. Methods Fluids 66 (6) (2011) 714–729.
[10] A. Staniforth, J. Côté, Semi-Lagrangian integration schemes for atmospheric models – a review, Mon. Weather Rev. 119 (9) (1991) 2206–2223.
[11] H. Whitney, Geometric Integration Theory, Princeton University Press, 1957.
[12] H. Weller, J. Thuburn, C.J. Cotter, Computational modes and grid imprinting on five quasi-uniform spherical C-grids, Mon. Weather Rev. 140 (8) (2012) 2734–2755.
[13] P.S. Peixoto, S.R.M. Barros, Analysis of grid imprinting on geodesic spherical icosahedral grids, J. Comput. Phys. 237 (2013) 61–78.
[14] G. Fasshauer, Positive definite kernels: past, present and future, Dolomit. Res. Notes Approx. 4 (2011) 21–63.
[15] E.L. Wachspress, A Rational Finite Element Basis, Math. Sci. Eng., vol. 114, Academic Press, 1975.
[16] A. Gillette, A. Rand, C. Bajaj, Error estimates for generalized barycentric interpolation, Adv. Comput. Math. 37 (2012) 417–439.
[17] A. Iske, M. Kser, Conservative semi-Lagrangian advection on adaptive unstructured meshes, Numer. Methods Partial Differ. Equ. 20 (3) (2004) 388–411.
[18] P.H. Lauritzen, R.D. Nair, P.A. Ullrich, A conservative semi-Lagrangian multi-tracer transport scheme (CSLAM) on the cubed-sphere grid, J. Comput. Phys. 229 (5) (2010) 1401–1424.
[19] A. Robert, A stable numerical integration scheme for the primitive meteorological equations, Atmos.-Ocean 19 (1981) 35–46.
[20] R.D. Nair, P.H. Lauritzen, A class of deformational flow test cases for linear transport problems on the sphere, J. Comput. Phys. 229 (23) (2010) 8868–8887.

[21] M. Floater, Mean value coordinates, Comput. Aided Geom. Des. 20 (1) (2003) 19–27.
[22] P. Alfeld, M. Neamtu, L.L. Schumaker, Bernstein-Bezier polynomials on spheres and sphere-like surfaces, Comput. Aided Geom. Des. 13 (4) (1996) 333–349.
[23] T. Langer, A. Belyaev, H.-P. Seidel, Spherical barycentric coordinates, in: Proceedings of the Fourth Eurographics Symposium on Geometry Processing, SGP'06, 2006, pp. 81–88.
[24] Q. Du, M.D. Gunzburger, L. Ju, Constrained centroidal Voronoi tessellations for surfaces, SIAM J. Sci. Comput. 24 (2003) 1488–1506.
[25] T.D. Ringler, J. Thuburn, J.B. Klemp, W.C. Skamarock, A unified approach to energy conservation and potential vorticity dynamics for arbitrarily-structured C-grids, J. Comput. Phys. 229 (9) (2010) 3065–3090.
[26] H. Tomita, M. Tsugawa, M. Satoh, K. Goto, Shallow water model on a modified icosahedral geodesic grid by using spring dynamics, J. Comput. Phys. 174 (2) (2001) 579–613.
[27] R. Walters, E. Hanert, J. Pietrzak, D.L. Roux, Comparison of unstructured, staggered grid methods for the shallow water equations, Ocean Model. 28 (1–3) (2009) 106–117.
[28] P. Solin, Partial Differential Equations and the Finite Element Method, Pure Appl. Math., Wiley, Hoboken, NJ, 2005.
[29] R. Klausen, A. Rasmussen, A. Stephansen, Velocity interpolation and streamline tracing on irregular geometries, Comput. Geosci. 16 (2012) 261–276.
[30] R.J. Renka, Interpolation of data on the surface of a sphere, ACM Trans. Math. Softw. 10 (1984) 417–436.
[31] C.L. Lawson, R.J. Hanson, Solving Least Squares Problems, Ser. Autom. Comput., Prentice-Hall, 1974.
[32] M.D. Buhmann, Radial Basis Functions, Cambridge University Press, New York, NY, USA, 2003.
[33] B.J.C. Baxter, S. Hubbert, Radial basis functions for the sphere, in: Recent Progress in Multivariate Approximation, Witten–Bommerholz, 2000, in: Int. Ser. Numer. Math., vol. 137, Birkhäuser, Basel, 2001, pp. 33–47.
[34] K. Hesse, Q.T. Le Gia, Local radial basis function approximation on the sphere, Bull. Aust. Math. Soc. 77 (2) (2008) 197–224.
[35] T. Ruppert, Vector field reconstruction by radial basis functions, Diploma thesis, Technical University Darmstadt, 2007.
[36] H. Wan, Developing and testing a hydrostatic atmospheric dynamical core on triangular grids, Ph.D. thesis, International Max Planck Research School on Earth System Modelling, Max Planck Institute for Meteorology, Hamburg, Germany, 2009.
[37] P. Rípodas, A. Gassmann, J. Förstner, D. Majewski, M. Giorgetta, P. Korn, L. Kornblueh, H. Wan, G. Zängl, L. Bonaventura, T. Heinze, Icosahedral shallow water model (ICOSWM): results of shallow water test cases and sensitivity to model parameters, Geosci. Model Dev. Discuss. 2 (1) (2009) 581–638.
[38] R. Schaback, Error estimates and condition numbers for radial basis function interpolation, Adv. Comput. Math. 3 (3) (1995) 251–264.
[39] G. Rosatti, D. Cesari, L. Bonaventura, Semi-implicit, semi-Lagrangian modelling for environmental problems on staggered Cartesian grids with cut cells, J. Comput. Phys. 204 (1) (2005) 353–377.
[40] F.J. Narcowich, J.D. Ward, Generalized Hermite interpolation via matrix-valued conditionally positive definite functions, Math. Comput. 63 (208) (1994) 661–687.
[41] B. Fornberg, J. Zuev, The runge phenomenon and spatially variable shape parameters in RBF interpolation, Comput. Math. Appl. 54 (3) (2007) 379–398.
[42] G. Fasshauer, M. McCourt, Stable evaluation of Gaussian radial basis function interpolants, SIAM J. Sci. Comput. 34 (2) (2012) A737–A762.
[43] B. Fornberg, C. Piret, A stable algorithm for flat radial basis functions on a sphere, SIAM J. Sci. Comput. 30 (1) (2008) 60–80.
[44] H. Miura, M. Kimoto, A comparison of grid quality of optimized spherical hexagonal–pentagonal geodesic grids, Mon. Weather Rev. 133 (10) (2005) 2817–2833.
[45] D.L. Williamson, J.B. Drake, J.J. Hack, R. Jakob, P.N. Swarztrauber, A standard test set for numerical approximations to the shallow water equations in spherical geometry, J. Comput. Phys. 102 (1) (1992) 211–224.
[46] J.L. McGregor, Economical determination of departure points for semi-Lagrangian models, Mon. Weather Rev. 121 (1993) 221–230.
[47] H. Ritchie, Semi-Lagrangian advection on a Gaussian grid, Mon. Weather Rev. 115 (2) (1987) 608–619.
[48] D. Shepard, A two-dimensional interpolation function for irregularly-spaced data, in: Proceedings of the 1968 23rd ACM National Conference, ACM'68, ACM, New York, NY, USA, 1968, pp. 517–524.
[49] R. Franke, G. Nielson, Smooth interpolation of large sets of scattered data, Int. J. Numer. Methods Eng. 15 (11) (1980) 1691–1704.
[50] R.J. Renka, Multivariate interpolation of large sets of scattered data, ACM Trans. Math. Softw. 14 (2) (1988) 139–148.
[51] R.J. Renka, Algorithm 660: QSHEP2D: Quadratic Shepard method for bivariate interpolation of scattered data, ACM Trans. Math. Softw. 14 (2) (1988) 149–150.
[52] R.J. Renka, Algorithm 661: QSHEP3D: Quadratic Shepard method for trivariate interpolation of scattered data, ACM Trans. Math. Softw. 14 (2) (1988) 151–152.
[53] G. Farin, Surfaces over Dirichlet tessellations, Comput. Aided Geom. Des. 7 (1–4) (1990) 281–292.
[54] H. Hiyoshi, K. Sugihara, Improving the global continuity of the natural neighbor interpolation, in: A. Lagan, M.L. Gavrilova, V. Kumar, Y. Mun, C.J.K. Tan, O. Gervasi (Eds.), ICCSA, vol. 3, in: Lect. Notes Comput. Sci., vol. 3045, Springer, 2004, pp. 71–80.
[55] R.J. Renka, Algorithm 773: SSRFPACK: Interpolation of scattered data on the surface of a sphere with a surface under tension, ACM Trans. Math. Softw. 23 (1997) 435–442.
[56] J. Thuburn, T.D. Ringler, W.C. Skamarock, J.B. Klemp, Numerical representation of geostrophic modes on arbitrarily structured C-grids, J. Comput. Phys. 228 (2009) 8321–8335.
[57] A. McDonald, Accuracy of multiply-upstream semi-Lagrangian advective schemes II, Mon. Weather Rev. 115 (7) (1987) 1446–1450.
[58] D.R. Durran, Numerical Methods for Fluid Dynamics: With Applications to Geophysics, Texts Appl. Math., vol. 32, Springer, 2010.